Draft version February 7, 2022
Typeset using LaTeX twocolumn style in AASTeX63

The Hydrogen-Poor Superluminous Supernovae from the Zwicky Transient Facility Phase-I Survey: II. Light Curve Modeling and Analysis

Z. H. Chen,[1] Lin Yan,[2] T. Kangas,[3] R. Lunnan,[4] J. Sollerman,[4] S. Schulze,[5] D. A. Perley,[6] T.-W. Chen,[4] A. Gal-Yam,[7] X. F. Wang,[1,8] K. De,[9] K. Taggart,[10] E. Bellm,[11] J. S. Bloom,[12,13] R. Dekany,[2] M. Graham,[9] M. Kasliwal,[14] S. Kulkarni,[14] R. Laher,[15] D. Neill,[9] and B. Rusholme[15]

[1]Physics Department and Tsinghua Center for Astrophysics (THCA), Tsinghua University, Beijing, 100084, China
[2]Caltech Optical Observatories, California Institute of Technology, Pasadena, CA 91125, USA
[3]The Oskar Klein Centre, KTH Royal Institute of Technology, Stockholm, Sweden
[4]The Oskar Klein Centre, Department of Astronomy, Stockholm University, AlbaNova, SE-106 91 Stockholm, Sweden
[5]The Oskar Klein Centre, Department of Physics, Stockholm University, AlbaNova, SE-106 91 Stockholm, Sweden
[6]Astrophysics Research Institute, Liverpool John Moores University, 146 Brownlow Hill, Liverpool L3 5RF, UK
[7]Department of particle physics and astrophysics, Weizmann Institute of Science, 76100 Rehovot, Israel
[8]Beijing Planetarium, Beijing Academy of Sciences and Technology, Beijing, 100044, China
[9]Cahill Center for Astrophysics, California Institute of Technology, 1200 E. California Blvd. Pasadena, CA 91125, USA
[10]Department of Astronomy and Astrophysics, University of California, Santa Cruz, CA 95064, USA
[11]DIRAC Institute, Department of Astronomy, University of Washington, 3910 15th Avenue NE, Seattle, WA 98195, USA
[12]Department of Astrophysics, University of California, Berkeley, CA 94720-3411, USA
[13]Lawrence Berkeley National Laboratory, 1 Cyclotron Road, MS 50B-4206, Berkeley, CA 94720, USA
[14]Division of Physics, Mathematics, and Astronomy, California Institute of Technology, Pasadena, CA 91125, USA
[15]IPAC, California Institute of Technology, 1200 E. California Blvd, Pasadena, CA 91125, USA

Submitted to APJ

ABSTRACT

We present analysis of the light curves (LCs) of 77 hydrogen-poor superluminous supernovae (SLSNe-I) discovered during the Zwicky Transient Facility Phase-I operation. We find that the majority (67%) of the sample can be fit equally well by both magnetar and ejecta-circumstellar medium (CSM) interaction plus ^{56}Ni decay models. This implies that LCs alone can not unambiguously constrain the physical power sources for SLSNe-I. However, 20% of the sample show clear signatures such as inverted V-shape or steep declining LCs, which are better described by the CSM+Ni model. The remaining 13% of the sample favor the magnetar model. Moreover, our analysis shows that LC undulations are quite common, observed in $34-62\%$ of the sample, depending on the strength of the undulations and the quality of the LCs. The majority (73%) of the undulations occur post-peak and "bumps"/"dips" each account for around half of the undulations. Undulations show a wide range in energy and duration, with median values and 1σ errors of $1.8\%^{+3.4\%}_{-0.9\%}$ $\mathrm{E_{rad,total}}$ and $26.2^{+22.6}_{-10.7}$ days, respectively. Our analysis of the undulation time scales suggests that intrinsic temporal variations of the central engine can explain half of the undulating events, while CSM interaction can account for the majority of the sample. Finally, all of the well-observed He-rich SLSNe-Ib have either strongly undulating LCs or the LCs are much better fit by the CSM+Ni model. These observations imply that their progenitor stars have not had enough time to lose all of the He-envelopes before the supernova explosions, and H-poor CSM are likely present in these events.

Keywords: Stars: supernovae: general

Corresponding author: Lin Yan, Z. H. Chen
lyan@caltech.edu, chenzh18@mails.tsinghua.edu.cn

1. INTRODUCTION

Superluminous supernovae (SLSNe), as one group of energetic stellar explosions, were first discovered in the mid-2000s (Quimby et al. 2007; Ofek et al. 2007; Smith et al. 2007). They are 10 − 100 times more luminous at the peak phase and evolve much slower than normal Type Ia and core-collapse supernovae (SNe). After the initial discoveries, it quickly became clear that the conventional radioactive decay model for normal core-collapse supernovae (CCSNe) can not explain the majority of SLSNe. Today, what powers these luminous and slowly evolving events remains unclear. Several mechanisms have been proposed, including interaction with circumstellar material (CSM, Chevalier & Irwin 2011; Chatzopoulos et al. 2012, 2013; Benetti et al. 2014), energy injection from a central engine such as a rapidly rotating neutron star (magnetar, Kasen & Bildsten 2010; Woosley 2010) or an accreting black hole (Dexter & Kasen 2013). Exotic, rare explosions were also proposed, such as electron-positron pair instability or pulsational pair instability supernovae theoretically predicted for extremely massive stars (PISN or PPISN, Rakavy & Shaviv 1967; Barkat et al. 1967; Woosley et al. 2007; Woosley 2017).

Magnetar models are flexible and often used to fit the light curves of SLSNe-I (*e.g.* Inserra et al. 2013; Nicholl et al. 2013). However, some observations already indicate that magnetar spin-down is not the only process which affects the LC luminosity and morphology for a SLSN-I, and there might be multiple processes affecting the optical emission. For example, the detection of late time Hα emission in three SLSNe-I indicates the presence of H-rich CSM shells ejected by the progenitor stars (Yan et al. 2015, 2017a). Another example is the discovery of Mg II emission lines resonant scattered by a H-poor CSM shell in the SLSN-I PTF16eh (Lunnan et al. 2018). Finally, the sharp V-shaped LCs of SN 2017egm are shown to be better fit by the ejecta-CSM interaction (CSI) model (Wheeler et al. 2017). Statistically, it is not clear what roles magnetars and CSI play for the population of SLSNe-I, and this needs further studies.

Temporal bumps or dips in SLSN-I LCs are known and have been observed in various objects (Nicholl et al. 2016; Yan et al. 2017a,b; Anderson et al. 2018; Lunnan et al. 2020). Such LC undulations can not be explained by a simple magnetar model. Previously, poor LC sampling and lack of uniform SLSN-I data sets have precluded detailed statistical analysis of LC undulations. A recent paper by Hosseinzadeh et al. (2021) has carried out a focused study using the published SLSN-I LCs from the literature. It discussed various possible physical drivers for this phenomenon but found no conclusive answers. The Hosseinzadeh et al. (2021) sample is compiled from multiple sources, which can introduce biases to undulation fractions and properties. The Zwicky Transient Facility (ZTF) Phase-I survey (Graham et al. 2019; Bellm et al. 2019a; Masci et al. 2019) has discovered and classified a large sample of SLSNe-I. The advantages of the ZTF LCs are the high cadence (3 days or less) and the excellent phase coverage at both early and late times (Bellm et al. 2019b). This provides a valuable opportunity to perform a statistical study on the LC undulations.

The detailed description of the ZTF survey, the SLSN-I sample and the complete photometric dataset are published in Chen et al. 2022, Paper I of this series. Paper I presented mostly the parameters which can be measured or directly computed from the data, such as redshift, extinction correction, K-correction, peak luminosity, peak phase, time scales (rise & decline), color, black-body temperature and bolometric luminosity.

This paper, Paper II, presents the detailed analysis of the LCs of the 77 of 78 ZTF SLSNe-I published in Paper I, excluding SN 2018ibb which is the focus of a separate paper (Schulze et al. in preparation). We focus on the LC morphology and various physical parameters derived from modeling, such as ejecta mass and explosion energy. Throughout the paper, apparent magnitudes are in the AB system, unless specified otherwise. We adopt a ΛCDM cosmology with $H_0 = 67.7\,\mathrm{km\,s^{-1}\,Mpc^{-1}}$, $\Omega_M = 0.307$ and $\Omega_\Lambda = 0.693$ (Planck Collaboration et al. 2016).

2. THE DATA

Our sample contains 77 SLSNe-I discovered from March 17, 2018 to October 31, 2020 by the ZTF survey. This sample covers redshifts of $z \sim 0.06 - 0.67$. The photometry data primarily comes from the ZTF in the g, r, i bands (Bellm et al. 2019a), and also includes additional data from other ground-based facilities (see Paper I for details) and *Swift* (Roming et al. 2005). Each event has been spectroscopically classified as described in Paper I. The majority of the spectra used for the velocity measurements are from the Double Beam Spectrograph (DBSP; Oke & Gunn 1983) and the Low Resolution Imaging Spectrometer (LRIS; Oke et al. 1995) mounted on the Palomar 200 inch (P200) and the Keck telescope respectively.

We divide the ZTF SLSN-I sample into three subsets – 'gold', 'silver', and 'bronze'. This is because some results depend on the LC phase coverage. The bronze class is defined by the number of epochs ≤ 10 in both g and r bands. The gold class is defined by the following two criteria: **[1]** no gap longer than 20 days in rest frame. **[2]** the LC covers phases which reach at least 0.5 and

1.0 mag below the peak luminosity pre- and post-peak, respectively. The gold class has 40 SLSNe-I and the bronze class has only 4. The remaining 33 events are in the silver class whose LCs have > 10 epochs in either g or r band, but do not meet both gold class criteria. Some analysis is performed only with the LCs in the 'gold' and 'silver' classes.

3. LIGHT CURVE MODELING

3.1. *Velocity Measurements at Peak Phases*

The width of a bolometric LC is closely related to the effective diffusion time scale, which describes the time photons take to travel through the ejecta material and is proportional to $(M_{ej}/V_{ej})^{1/2}$. When modeling LCs to derive ejecta masses and other physical parameters, it reduces the number of free parameters and uncertainties if V_{ej} can be constrained separately from optical spectra. Here V_{ej} is approximated with the photospheric velocity at peak phases (Arnett 1982; Kasen & Bildsten 2010; Nicholl et al. 2017a).

We use three different ways to measure the photospheric velocities. The first method is to use Fe II $\lambda\lambda\,4924, 5018, 5169$ absorption lines as tracers. Liu et al. (2016) and Modjaz et al. (2016) have shown that this method can derive robust measurements for stripped-envelope SNe and the spectral template-matching technique can mitigate blended Fe II lines for high-velocity events such as SNe Ic-BL. The second type of spectral tracers is the five O II absorption lines at $3737 - 4650$ Å, the hall-mark features for SLSNe-I at early phases (Quimby et al. 2011). These are useful for velocity measurements as shown by Quimby et al. (2018); Gal-Yam (2019). The third method is to cross-correlate the spectra of our events with spectral templates from several well-studied SLSNe-I, and estimate the relative spectral shifts, thus their relative velocities.

Using the template-matching code from Liu et al. (2016) and Modjaz et al. (2016)[1], we measure 87 velocities with errors from Markov Chain Monte Carlo (MCMC) for 47 SLSNe-I using Fe II features. Note that the pre-peak Fe II velocity can be underestimated due to the contamination of Fe III as illustrated in Liu et al. (2016). The spectra are cleaned by removing the narrow host emission lines, then smoothed and divided by the continua. Assuming the five absorption features have the same velocity, we derive the spectral shifts by fitting the local minima using the least-squares method. The errors are calculated from the co-variance matrix. The five O II features do not have the same strength, with O II $\lambda\lambda\,4358, 4651$ (features A & B) the strongest. For some spectra, we fit only 2 to 4 significant features since the others are too weak. We derive 41 velocities at phases -43 to $+14$ days for 33 SLSNe-I using O II tracers. ZTF18abshezu has very strong O II features from -38.6 to $+11.7$ days and we highlight its evolution in Figure 1.

For some events in our sample, their Fe II and O II lines are not clearly identified, especially when Mg I $\lambda\lambda\,3829, 3832, 3838$ or Ca II $\lambda\lambda\,3934, 3969$ may be present. For these spectra with ambiguous feature identifications, we match them with three well-observed SLSNe-I, PTF12dam, SN 2011ke and SN 2015bn near peak phases (Inserra et al. 2013; Quimby et al. 2018; Nicholl et al. 2013, 2016). We record the velocities derived from the five best-matching templates and use their mean value as our final result and the standard deviation as the error.

In total, we are able to measure photospheric velocities near peak phases for 56 events. The remaining events do not show clear Fe II or O II features or do not have sufficient spectra at the right phases. The measured velocities V_{ph} are listed in Table A1.

Figure 1 shows the measured velocities as a function of phase as well as the histograms of velocity distributions. The shaded region marks the early (phase < -20 days) and late (phase $> +30$ days) time region. The histogram distributions in the right panel show that near the LC peak (-20 days $\lesssim$ phase $\lesssim +30$ days), the Fe II velocity has a median value of 14,020 km s^{-1}, whereas the median O II velocity is only 9700 km s^{-1}. Considering the velocities from both ionic species, the median peak photospheric velocity is about 11,490 km s^{-1} for our sample of SLSNe-I. A similar trend is found for PTF12dam, where the O II velocity at peak is 3000 km s^{-1} slower than that of Fe II (Quimby et al. 2018). This is an illustration that Fe^{+} ions need lower ionization temperatures and are located at the outer layers of ejecta, thus having higher velocities, whereas the O^{+} ions tend to be in the inner ejecta regions with lower velocities. To avoid possible biases caused by the choice of binning for the histgram distribution, we apply kernel density estimation on all the histograms in this paper (shown as the solid lines in the histograms) using a Gaussian kernel offered by the machine learning package Scikit-learn (Pedregosa et al. 2011).

As discussed earlier, the effective photon diffusion time scale is proportional to $(M_{ej}/V_{ej})^{1/2}$, so the LC rise times should have a similar dependence. Figure 2 displays the photospheric velocities versus the rise times ($t_{rise,10\%}$ from Paper I), in comparison with the data from a broad-lined SN Ic (SN Ic-BL) sample (Taddia

[1] https://github.com/nyusngroup/SESNspectraLib

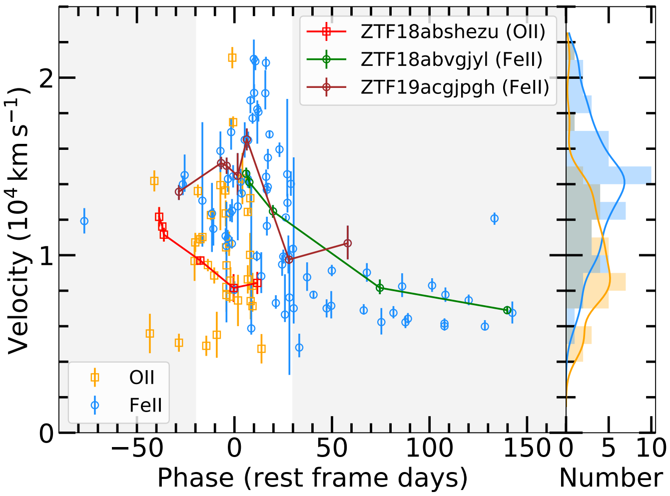

Figure 1. Photospheric velocities versus phases. We mark the early (phase < -20 days) and late (phase $> +30$ days) time region with shaded area. The velocity evolutions of three events with good phase coverage are highlighted in different colors. The right panel shows the distribution of Fe II and O II velocities near peak phases in the white area. The blue and orange solid lines show the kernel density estimation of the distributions, respectively.

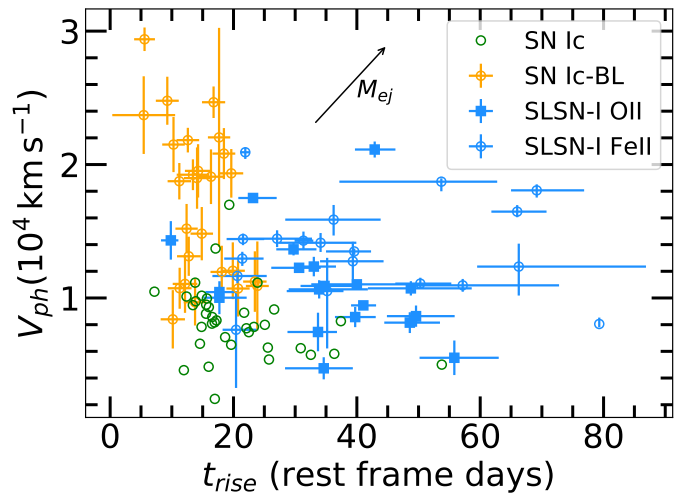

Figure 2. Photospheric velocities versus LC rise times. The SLSN-I velocities measured from Fe II and O II are marked with different symbols in blue, while the data of broad-lined SNe Ic (SNe Ic-BL) and normal SNe Ic are marked with orange and green dots (from Taddia et al. 2019; Barbarino et al. 2021), respectively. We mark the direction of increasing M_{ej} with the black arrow.

et al. 2019) and a normal SN Ic sample (Barbarino et al. 2021). The rise times of our sample are measured in rest-frame g band, while those of the SNe Ic are in the observed r band, which correspond roughly to the rest-frame wavelengths slightly longer than that of g-band because most of these SNe Ic are at lower z than our sources. We do not attempt to correct for this inconsistency. The velocities of the SNe Ic were measured from Fe II in the same way as ours. We test for correlations using the Spearman rank correlation coefficient and find that SNe Ic (including both SNe Ic-BL and normal SN Ic) show a strong negative correlation ($\rho = 0.46$, $p \lesssim 10^{-4}$) between the rise times and the photospheric velocities, *i.e.* slow evolving events having lower velocities. However, the correlation is not significant ($\rho = 0.18$) when also including SLSNe-I. This is possibly because the SLSN-I velocities are measured in a relatively wide range (-20 days $\lesssim$ phase $\lesssim +30$ days), instead of strictly at peak. If we instead use the SLSN-I velocities from the LC modeling in §3.2, the correlation is significant ($\rho = 0.33$, $p < 10^{-3}$), but still weaker than that of the SNe Ic alone. This may suggest that the spread in ejecta masses is larger for SLSNe-I than for SNe Ic. On average, the velocities of SLSNe-I ($\sim 12000\,\mathrm{km\,s^{-1}}$) are higher than for normal SNe Ic ($\sim 8000\,\mathrm{km\,s^{-1}}$) but lower than for SNe Ic-BL ($\sim 17000\,\mathrm{km\,s^{-1}}$), which is consistent with Liu et al. (2017b).

3.2. *Light Curve Modeling*

3.2.1. *Model setup*

One of the primary science goals in this paper is to set constraints on the power sources for the luminous optical emission seen in the SLSNe-I. The open source software `MOSFiT` (Guillochon et al. 2018) is used to model the LCs of 70 (out of 77) events in the gold and silver class with good phase coverage. We exclude 3 silver and 4 bronze events with poorly sampled data before the peak. For 9 events, we exclude the faint data obtained at either very early or late phases which apparently cannot be fit by a single model together with their peak. Three special events, *i.e.* ZTF20aadzbcf, ZTF20aaifybu and ZTF19acbonaa, show a strong secondary peak. We limit the range of LC modeling to their primary peaks only. The input LC data are corrected for Galactic extinction, but not the host extinction, which is a free parameter in `MOSFiT`. The input LC data are binned into one-day bins.

We run `MOSFiT` via Dynamic Nested Sampling (`dynesty`, Speagle 2020) and request that both the initial $\Delta\log_{10}Z$ in the static phase and the KL-divergence criterion in the dynamic phase equal 0.02. We choose two commonly used models, *i.e.* the magnetar (*slsn* model in `MOSFiT`, Kasen & Bildsten 2010; Nicholl et al. 2017b) and the CSM+Ni (*csmni* model in `MOSFiT`, Chatzopoulos et al. 2013). For the CSM+Ni model, we fit both a constant density ($s = 0$) and a wind-like density ($s = 2$) profile. The key parameters are listed in

Table A2. Each free parameter has a prior distribution defined by MOSFiT. These prior distributions can be modified for specific dataset. For example, for most of our sources, the photospheric velocities are measured from the spectra, and we set the V_{ej} prior to a flat distribution from $0.7-1.3$ times the measured peak velocities. For some events with only post-peak velocities, we increase this multiplication factor to 1.6 when setting the upper limit of the V_{ej} prior. For the events without measured velocities, we use a constant velocity range of $3000-25000\,\mathrm{km\,s^{-1}}$, allowing MOSFiT to estimate velocities from the LC fitting.

For the magnetar model, we set the angle between the magnetic field and the spin axis $\theta_{PB} = \pi/2$. The output B-field from the MOSFiT is only the perpendicular component $B_\perp$, which relates to the total magnetic field through $B_{total} = B_\perp/\sin\theta$. For the priors of the other parameters in the magnetar model, we use probability distributions similar to the ones in Nicholl et al. (2017b). For the CSM+Ni model, we use the default distributions of CSM mass and CSM shell density. We set the mass ratio of ^{56}Ni to be less than 50%, the radius of the progenitor star to have a range from 0.01 to 100 AU and the opacity κ from 0.05 to 0.34 $\mathrm{g\,cm^{-2}}$. Except for κ, the other parameters common to both the magnetar and CSM+Ni models have the same prior distributions for consistency. Another parameter – γ-ray photon leakage parameter κ_γ – has a constant prior of $\log_{10}\kappa_\gamma$ between (-2, +2), as used in Nicholl et al. (2017a). We do not find necessary to use a wider range of the prior for κ_γ, as we discuss the κ_γ distribution for the full sample below.

Finally, for each run, MOSFiT outputs a large number of possible model LCs with different weights based on dynesty. We use the weighted median LC as the final model LC and evaluate the error by 16% and 84% percentiles. In a small number of cases, MOSFiT converges to different outputs with the same priors for different runs. This is primarily due to the large parameter space where the convergence could be at local minimum. In these cases, we ran MOSFiT several times and use the best result indicated by the largest $\log_{10}Z$ values.

3.2.2. *Importance of ejecta-CSM interaction in SLSNe-I*

One basic question is which of these two models fits the data better. To quantify this, we use the reduced χ^2 parameter using the numbers of fitted parameters – 11 and 12 for the magnetar and the CSM+Ni model respectively. A small number of data points from P200 and LT have very high signal-to-noise ratio (SNR) and small magnitude errors. To prevent excessive weights on these data, we set the smallest error to 0.01 mag when calculating the χ^2 parameter.

Figure 3 shows the χ^2_{Mag} computed for the magnetar model versus the χ^2 difference between the CSM+Ni model and the magnetar model. For the CSM+Ni model, we choose either $s = 0$ or $s = 2$ depending on which χ^2 is smaller. The large absolute χ^2 values can be due to underestimated photometric errors and the LC undulations. For example, the strongly undulating event ZTF19acgjpgh, located at the very right of Figure 3, can not be properly fit by either model. According to $\Delta\chi^2/\overline{\chi^2} = (\chi^2_{CSM} - \chi^2_{Mag})/[(\chi^2_{CSM} + \chi^2_{Mag})/2]$, we find that only a small fraction of the 70 SLSN-I events clearly prefer one model, with 14 events better fit by the CSM+Ni model and 9 by the magnetar model. The majority ($47/70 = 67\%$) of the sample can be equally well fit by both models ($|\Delta\chi^2/\overline{\chi^2}| < 35\%$). This indicates that LCs alone can not unambiguously distinguish between these two energy sources.

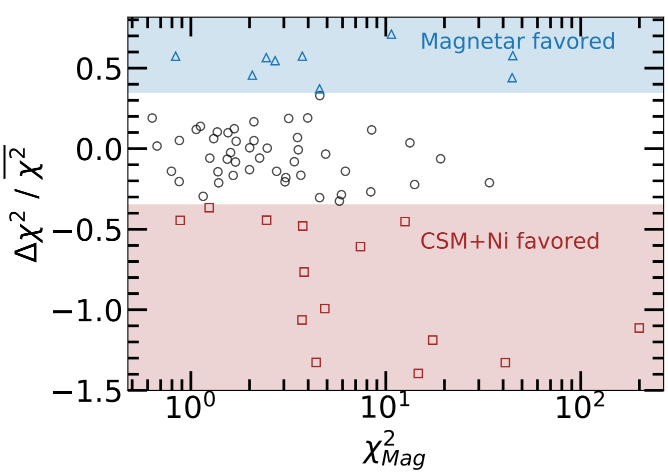

Figure 3. Reduced χ^2 values of the magnetar and CSM+Ni modeling. Y-axis shows the relative differences of χ^2 between these two models. The red area marks the region where the events are better fit by the CSM+Ni model, *i.e.* $\Delta\chi^2/\overline{\chi^2} < -35\%$, while the blue area marks the magnetar-favored region, *i.e.* $\Delta\chi^2/\overline{\chi^2} > 35\%$. The events in different areas are labeled with different symbols.

The 14 events favoring the CSM+Ni model have several distinct features. First, some LCs show a steep flux drop after the primary peak, *e.g.* ZTF18aajqcue and ZTF20abisijg. This steep change of LC slope generally can not be reproduced by the magnetar model, as revealed by the poor fits (see the dashed lines) in Figure 4. However, the CSM+Ni model with a wind-like ($s = 2$) or constant ($s = 0$) density profile does much better (solid lines in Figure 4). The rapid decline has a simple physical explanation where the forward shock has run through the CSM (Chatzopoulos et al. 2012). Second, some LCs have inverted V-shaped evolution, *i.e.* linear rise and decline with a sharp peak, *e.g.* ZTF19aaqrime and ZTF20aauoudz. This type of LCs can also be better fit by the CSI model, with a constant density CSM shell ($s = 0$), as previously noted by Chatzopoulos et al. (2013) and Wheeler et al. (2017). This is consistent with the finding shown in Paper I that most events favoring the CSM+Ni model tend to have longer rise times but shorter decay times compared with the other SLSNe-I.

We infer that the **minimum** fraction of CSM+Ni powered SLSNe-I in our sample is 20% (14/70). Half (7) of these events have smooth LCs, but clearly prefer the CSM+Ni model. Our analysis in §4 shows that CSI likely plays an important if not dominant role in all sources with LC undulations. In §4, we quantitatively identify 24 events from our sample have either weak or strong undulations. If taking into account all 24 undulating sources plus the 7 events with smooth LCs and favoring the CSM+Ni model, the fraction of CSM powered events can be as high as $33 - 53\%$ (31/73) at a confidence level (CL) of 95% (Gehrels 1986). Such a high fraction implies that H-poor (some also He-poor) CSM around SLSNe-I is quite common, and that CSI is much more prevalent than previously thought.

3.2.3. *Physical Parameters Derived from Model Fittings*

We compare the peak luminosities and temperatures derived from `MOSFiT` with that from the SED fitting in Paper I, and find that they are largely consistent with each other, with small offsets of $6^{+9}_{-14}\%$ and $-1^{+11}_{-12}\%$ respectively. Figure A1 displays several relations between the derived parameters, similar to Nicholl et al. (2017b, their Figure 6). E_k is derived from M_{ej} and V_{ph}, assuming $E_k = 0.3 M_{ej} V_{ph}^2$. This relation is valid for a homogeneous density profile, and also adopted for the CSM+Ni model. Our E_k values are thus somewhat lower than those derived by Nicholl et al. (2017b) which used $E_k = 1/2 M_{ej} V_{ph}^2$. The overall distributions of $P, B_\perp, M_{ej}$, and E_k are similar to the results in Nicholl et al. (2017b); Blanchard et al. (2020); Hsu et al. (2021). As found by Blanchard et al. (2020) and Hsu et al. (2021), M_{ej} shows a strong negative correlation ($\rho = -0.58,\ p < 10^{-6}$ in our sample) with magnetar spin period P, indicating that SLSNe-I with smaller ejecta masses require less central power with slower spinning neutron stars.

Figures 5 and 6 show the distributions of the key parameters from the magnetar model ($P, B_\perp, M_{ej}$, and E_k) and the CSM+Ni model ($M_{ej}, M_{CSM}, M_{\rm Ni}$, and E_k). The median values and the 1σ errors (16% and 84% percentiles) of the key parameters from the two models are listed in Table 1. The CSM+Ni model we use in `MOSFiT` is based on the semi-analytic model from Chatzopoulos et al. (2012, 2013). However, it has been shown that the semi-analytic model and hydrodynamic simulations can produce inconsistent results assuming the same CSM structure (Moriya et al. 2013; Sorokina et al. 2016). The quantitative value of the CSM parameters from the CSM+Ni model could be uncertain.

Table 1. Key modeling parameters

Parameter	Magnetar	CSM+Ni
P (ms)	$2.35^{+2.03}_{-0.72}$	-
$B_\perp$ (10^{14} G)	$0.97^{+0.76}_{-0.67}$	-
M_{CSM} ($M_\odot$)	-	$6.07^{+8.09}_{-3.82}$
$M_{\rm Ni}$ ($M_\odot$)	-	$0.21^{+3.54}_{-0.19}$
M_{ej} ($M_\odot$)	$4.92^{+4.24}_{-2.19}$	$10.44^{+25.88}_{-9.08}$
E_k (10^{51} erg)	$2.41^{+2.08}_{-1.03}$	$5.58^{+13.72}_{-4.82}$

Compared with the magnetar model, the M_{ej} estimates from the CSM+Ni model are significantly higher. The final mass of the progenitor star M_{prog} is estimated by summing up M_{ej} and M_{NS} for the magnetar model, and M_{ej}, M_{CSM} plus a typical neutron-star mass ($1.4\,M_\odot$, Lattimer & Prakash 2007) for the CSM+Ni model. Note that the progenitor mass calculated with this method is just a lower limit. Figure 7 shows the mass estimates for the 47 events which are equally well fit by both the magnetar and CSM+Ni models. The progenitor mass derived from the magnetar model has a median value of $6.36^{+4.80}_{-1.61}\ M_\odot$ while it is $20.52^{+27.04}_{-10.99}\ M_\odot$ from the CSM+Ni model.

Assuming a stellar population with low metallicity (metal fraction 10% solar, *i.e.* $1 - 2 \times 10^{-3}$), we estimate the zero-age-main-sequence (ZAMS) mass using *PARSEC* (Bressan et al. 2012). A ZAMS mass of $20 - 37\ M_\odot$ is needed for the magnetar model while $32 - 150\ M_\odot$ is required for the CSM+Ni model. It is not surprising that the predicted progenitor and ZAMS masses for the CSM+Ni model are much larger. This reflects the fact that the CSM+Ni model needs both larger ejecta and CSM masses in order to supply sufficient energy, as also noted previously by Chatzopoulos et al. (2013). More importantly, the high ZAMS values for the CSM+Ni model are in the regime ($70 - 140 M_\odot$) where Pulsational electron-positron Pair-Instability Supernova are expected to explode (PPISN; Woosley 2017). PPISN events will also experience violent episodic mass losses. This may naturally explain the presence of substantial amount of CSM.

Another parameter which can significantly impact the ejecta mass estimates is κ_γ, the γ-ray photon leakage parameter. The smaller κ_γ values, the faster LC de-

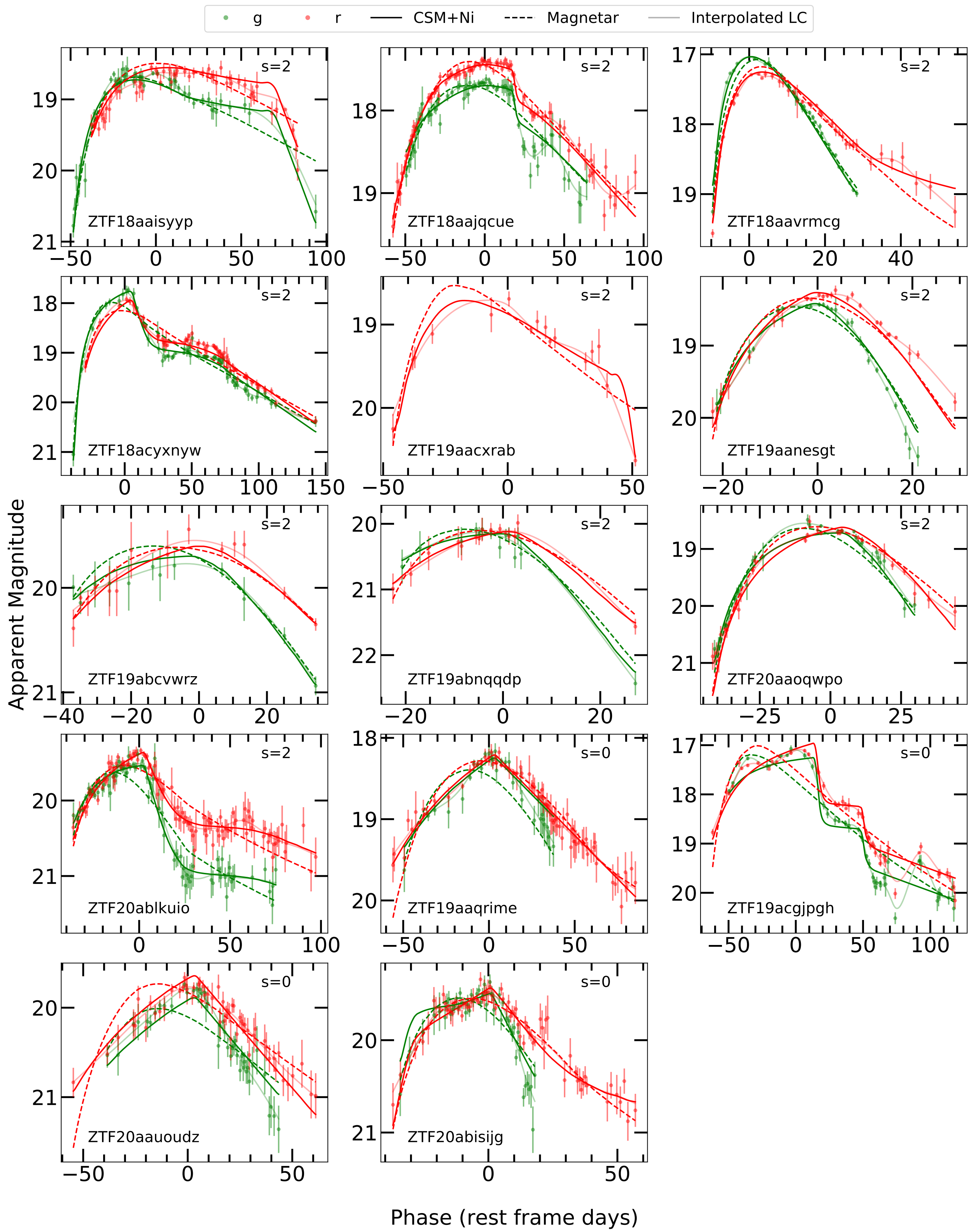

Figure 4. The 14 events best fit by the CSM+Ni model. CSM+Ni model, magnetar model and GP interpolated LCs are plotted with solid lines, dashed lines and translucent lines, respectively. The type of CSM structure, constant density ($s = 0$) or wind-like ($s = 2$), is labeled at the top right corner. The data in shaded region are masked out during the LC modeling.

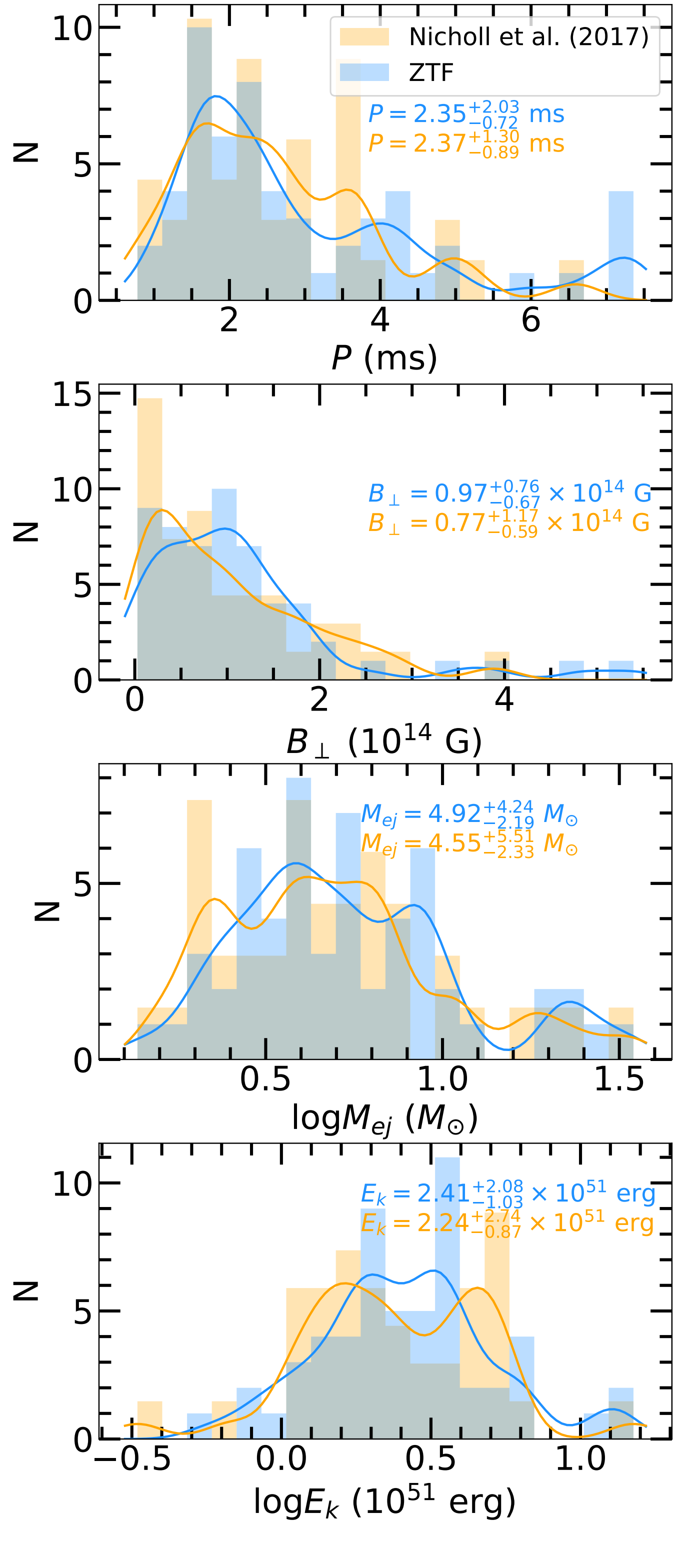

Figure 5. Distribution of a series of important parameters $(P, B_\perp, M_{ej}, E_k)$ in the magnetar model. The blue color indicates the distribution and median value for the 56 (9+47) SLSN-I fit by the magnetar models (9 events favor the magnetar models, and 47 can be fit equally well by both the CSM and magnetar models). Those from Nicholl et al. (2017b) are shown in orange for comparison (total number is normalized to that of ZTF sample). The solid lines show the kernel density estimation of the distributions.

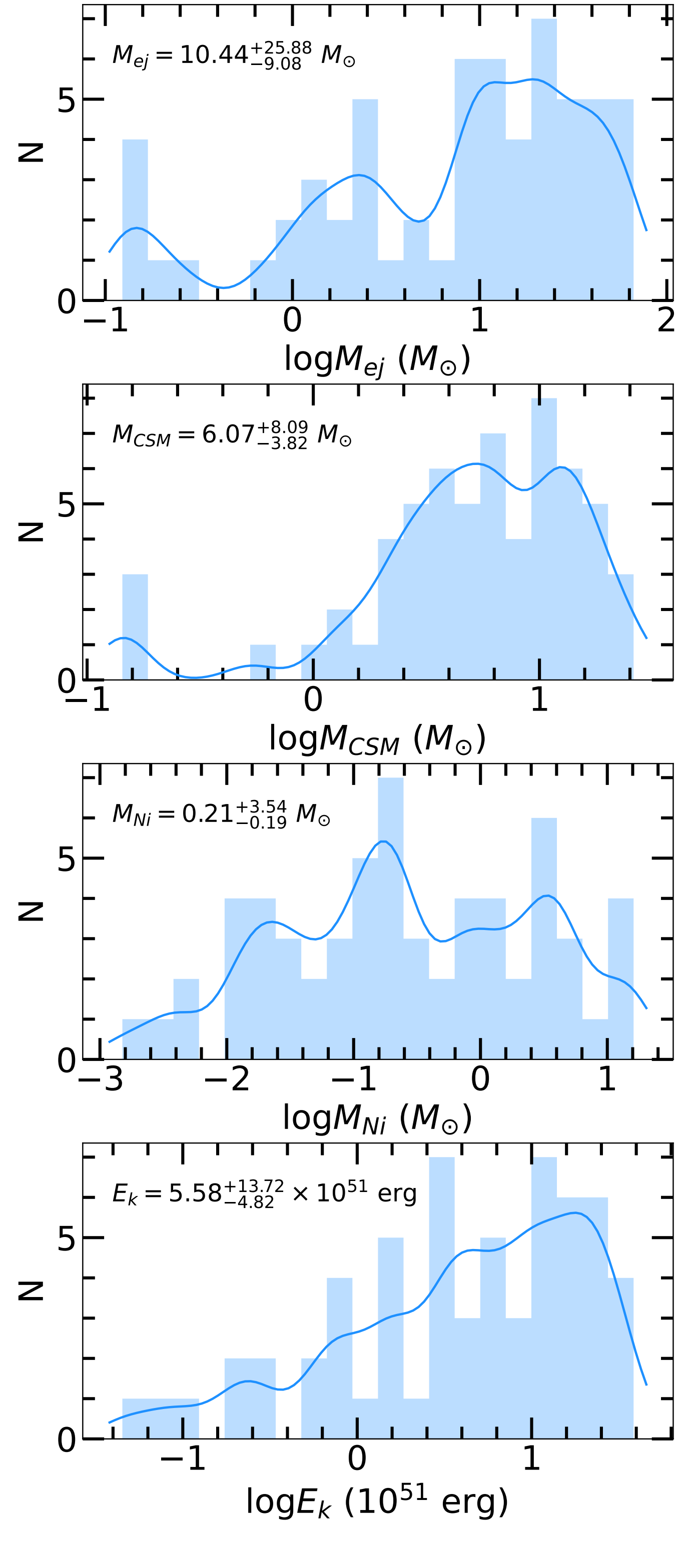

Figure 6. Distribution of key parameters $(M_{ej}, M_{CSM}, M_{\rm Ni}, E_k)$ derived for the CSM+Ni model. Here we include the 14 SLSNe-I favored by the CSM+Ni models and the 47 events which can be fit equally well by both the CSM and magnetar models. The solid lines show the kernel density estimation of the distributions.

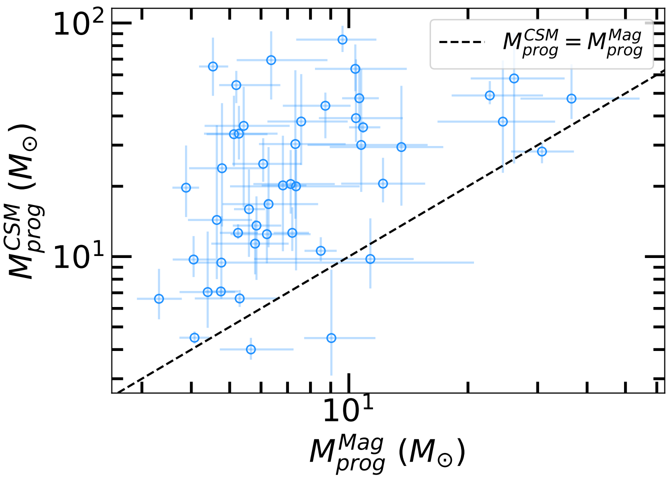

Figure 7. Progenitor mass M_{prog} derived from the magnetar model (x-axis) and from the CSM+Ni model (y-axis) for the 47 SLSNe-I for which both models are equally good fits.

cays and as compensation, the larger ejecta masses are needed to fit the late-time LCs. The `MOSFiT` derived $\log_{10}\kappa_\gamma$ values for the majority of our sample is > -1.7, with a small fraction ($4-10$ of 70 for different models) having $-1.95 < \log_{10}\kappa_\gamma < -1.7$.

Recently, Vurm & Metzger (2021) carried out three-dimensional Monte Carlo radiative transfer calculations on SLSNe-I using the magnetar model and showed that $\log_{10}\kappa_\gamma = -2$ is an extremely low value for phase < 300 days (see their Figure 10). Such low κ_γ requires highly efficient dissipation of the magnetic field or that the spin-down luminosity decays significantly faster than the canonical dipole rate $\propto t^{-2}$ in a way that coincidentally mimics gamma-ray escape. We conclude that our assumed prior for κ_γ is sufficient and we do not need to explore a wider range of the distribution.

4. LIGHT CURVE MORPHOLOGIES

4.1. *Early double-peak Light Curves*

Some SLSNe-I have a weak bump in the early phase, *e.g.* SN 2006oz (Leloudas et al. 2012), LSQ14bdq (Nicholl et al. 2015a), DES14X3taz (Smith et al. 2016) and SN 2018bsz (Anderson et al. 2018). Nicholl & Smartt (2016) speculated that most SLSNe-I may have such early bump features. This was shown to be incorrect by the SLSN-I sample from the Dark Energy Survey (DES) which has very deep photometric limits (Angus et al. 2019). Of the 12 DES SLSNe-I with pre-peak LCs, only 4 showed such a precursor bump.

We also search for early bump features in our SLSN-I sample. We bin the LC data into one-day bins and include only data with SNR > 3 in our analysis. We focus on the 15 events which have very early and deep observations after the explosion. These 15 events have at least 4 epochs of pre-peak data which are 1.5 magnitudes fainter than their main peaks. We find that only three events, ZTF19aarphwc, ZTF19abpbopt and ZTF19abzoyeg, show reliable early-peak features. This corresponds to a fraction of $6-44\%$ (3/15, CL= 95%). This is consistent with the the observed fraction (*i.e.* 4/12) in Angus et al. (2019). The LCs of these three SLSNe-I are shown in Figure 8, together with the rest-frame g-band LCs of SN 2006oz, LSQ14bdq and DES14X3taz. The early bumps are detected only in rest-frame g band (observed r band) in ZTF19aarphwc and ZTF19abzoyeg, whereas in ZTF19abpbopt the initial peak is present in both the g- and r-band LCs (rest-frame). The early bump is fit by a second-order polynomial whereas the primary peak is fit by the GP method. We define the width of the first peak as the time interval between the two phases when the LC is 2 magnitudes fainter than the peak. The measured time widths and the absolute magnitudes of the first peak are listed in Table 2. The widths of the early bumps are comparable to the predictions of $10-20$ days from the shock cooling models by Piro (2015).

Table 2. The properties of early bump features

Name	Filter[a]	Width (days[a])	M_{bump} (mag)
ZTF19aarphwc	g	16.58	-20.30
ZTF19abzoyeg	g	18.91	-20.33
ZTF19abpbopt	g	9.08	-19.78
ZTF19abpbopt	r	11.08	-19.47
SN 2006oz	g	10.04	-19.26
LSQ14bdq	g	13.42	-20.05
DES14X3taz	g	19.06	-19.46

[a]Rest frame.

An alternative model – magnetar shock breakout through pre-explosion ejecta (Kasen et al. 2016) – can also explain the early bumps of SLSNe-I. In these models, the early bumps are more obvious if the power engine for the primary peak is inefficiently thermalized at the first $15-43$ days after the explosion (Kasen et al. 2016; Liu et al. 2021). The early bumps in ZTF19abpbopt and ZTF19abzoyeg are shallower, which perhaps implies that their magnetar energy thermalization is relatively more efficient.

It is worth noting that among the double-peaked SLSNe-I, ZTF19abpbopt is peculiar, and has a narrow early-bump width (9.08 days) and a short main peak

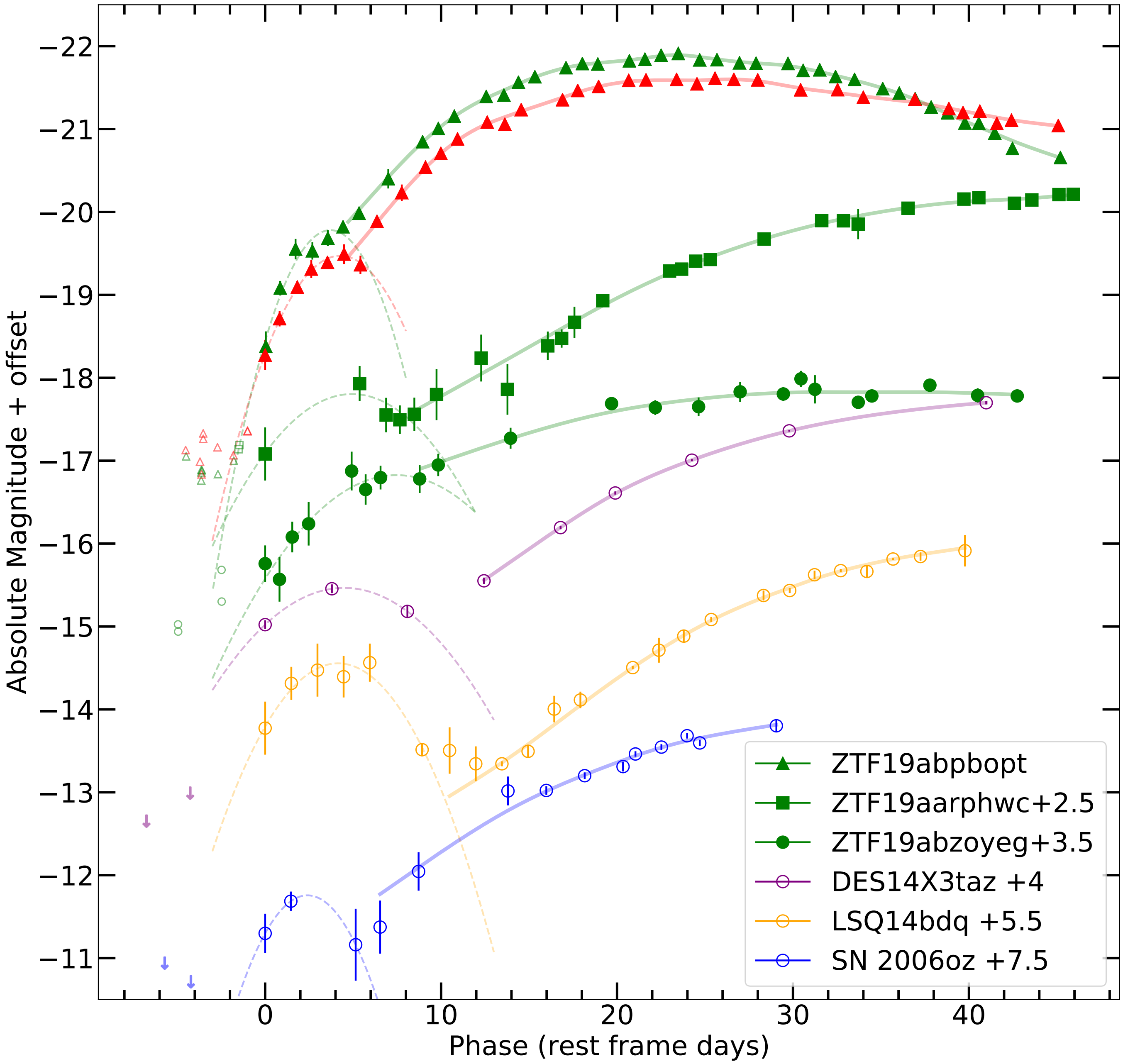

Figure 8. Early bump features of three ZTF SLSNe-I and archival SLSNe-I in rest-frame g band. The 3σ detections of ZTF events are presented in green solid points while the upper limits are in hollow points with the same markers. ZTF19abpbopt shows early bumps in both rest-frame g and r bands, and we highlight its r-band LC in red. Solid lines show the GP model fits of the LCs. Dashed lines show the second-order polynomial fitting applied to the early bump features.

rise time ($\lesssim 25$ days). This makes it the fastest-evolving SLSNe-I with early bumps up to date. So far most SLSNe-I with early bumps are slow events (rise time $\sim 33-100$ days, Inserra 2019). This could be due to the observational selection bias since fast-evolving events with narrow early bumps can be easily missed by supernova surveys unless with high cadence and early sensitive detections.

4.2. *Undulations in the light curves*

Our large sample of SLSNe-I and their LCs with excellent phase coverage provide a great opportunity to examine the LC undulation properties systematically. We perform analysis of the LCs of the 73 events in the gold and silver subclasses. The four events in the bronze class are excluded because of the sparse phase coverage of the LCs. To quantitatively identify the undulations, we compute the residual LC (RLC) by subtracting out a smooth baseline (produced by the MOSFiT models) from the observed LC. The observed data is interpolated using the GP regression. One example is shown in Figure 9, where the RLC is shown in the bottom panel including errors due to both the GP interpolation and the baseline model. In the RLC, the strength and phase of the "bump" and "dip" can be mathematically determined by their local maximum and minimum, marked as black dots in Figure 9. The maximum amplitude between the adjacent minimum and maximum, recorded as $\Delta \mathrm{Mag}^{max}_{RLC}$, defines how much the LC deviates from the smooth baseline LC. The hatched area shows the time interval of the undulation, and the detailed properties of the LC undulations are discussed in §4.3.

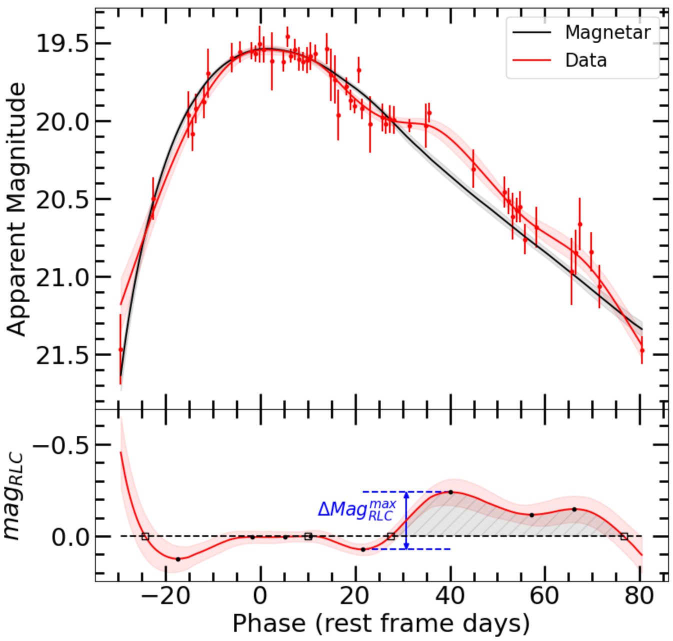

Figure 9. An example of the LC undulation measurements. The upper panel shows the r-band LC of ZTF19aamhhiz. The GP interpolated LC is plotted with a red line while the black line represents the LC fit with the magnetar model. The pink and grey shaded areas represent their 1-sigma errors, respectively. The lower panel shows the residual LC (RLC) with 1σ errors from the GP and the magnetar model. The black points represent the local extrema and the blue vertical bar shows $\Delta \mathrm{Mag}^{max}_{RLC}$, the largest magnitude change between two adjacent extrema of the RLC. The black squares mark the zero points of the RLC. The time duration and energy of the undulations are measured from the intervals between two adjacent zero points as shown in the hatched area.

One key element in computing the RLC is how to define the smooth baseline LC. Polynomial or GP regression fitting can produce smooth baselines, but they are also easily influenced by intrinsic bumps and dips. These two methods can in principle be applied to the rebinned LCs to smooth out the intrinsic LC variations. However, to achieve optimal results, both methods rely heavily on manual labor. They are not the best choice for our large sample. Instead, we adopt physical model LCs to define the smooth photometric evolution, derived by running MOSFIT on the LCs (see §3 for details). Here we summarize the LC fitting results from §3 again. Of the 70 SLSNe-I with sufficient data, 14 events are better fit by CSM+Ni model, 9 are better fit by magnetar model. The rest 47 events can be equally well fit by both models and we use the magnetar model as their smooth baselines. The last three events (ZTF18abrzcbp, ZTF18abvgjyl and ZTF19abkfshj) are poorly sampled before peak phases, and their LCs do not show significant bump or dip features. Their baseline LCs are defined by a third-order polynomial fit.

To avoid artificial bumps/dips produced by the interpolation in the absence of data, we require each extremum in the RLC to have at least two nearby data points within 10 days. To minimize the impact of occasional photometric outliers, we require the time separation between extrema to be > 5 days. The significance of each RLC amplitude is set by its SNR $= |\Delta \mathrm{Mag}^{max}_{RLC}|/1\sigma$, where the 1σ error includes the uncertainty from MOSFiT. The SNR value determines the significance of each undulation.

Figure 10 shows $\Delta \mathrm{Mag}^{max}_{RLC}$ versus SNR. $\Delta \mathrm{Mag}^{max}_{RLC}$ reflect the luminosity ratio between the bumps/dips relative to the baselines, so we also label the luminosity percentage at the top x-axis of Figure 10, where +26% and −21% correspond to ± 0.25 mag, respectively. We define a strong undulation as SNR ≥ 3 and $|\Delta \mathrm{Mag}^{max}_{RLC}| \geq 0.25$ mag, and a weak undulation as SNR ≥ 3 and $0.1\,\mathrm{mag} < |\Delta \mathrm{Mag}^{max}_{RLC}| < 0.25$ mag. A total of 24 events have LC undulations with SNR ≥ 3. Of these, 16 are strongly undulating sources and 8 weak ones. ZTF18acapyww is manually moved from strongly undulating sources to weak ones due to lack of sufficient data around the undulation. We list the strongly and weakly undulating events in Table 3. The LCs of strongly undulating sources are shown in Figure 11, and those of the 8 weakly undulating events are presented in Figure 12.

Based on the above analysis, the fraction of undulating LCs is estimated to be 33% (24/73). If counting only the strongly undulating events, this fraction is 22% (16/73) while the fraction of weak undulations is 11% (8/73). However, the LCs of the silver events usually do not have complete phase coverage and the undulation can be missed due to the lack of data. If we examine

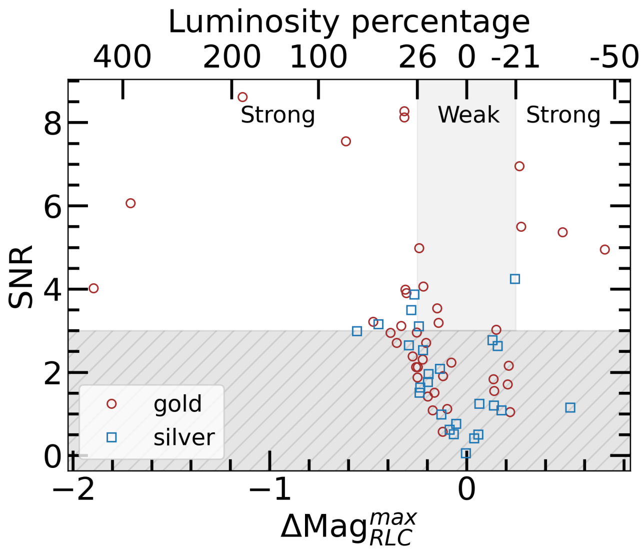

Figure 10. The maximum amplitude of the undulation versus the significance. X-axis shows $\Delta\mathrm{Mag}_{RLC}^{max}$, the maximum amplitude of the RLC (See Figure 9) and Y-axis is the SNR, *i.e.* the amplitude divided by the uncertainty. The energy percentage of the bump/dip relative to the smooth baseline LC is computed and labeled at the top. The region of SNR<3 is marked as the hatched region and the weak undulation amplitude region with $|\Delta\mathrm{Mag}_{RLC}^{max}| < 0.25$ mag is in shaded area. Events in the gold and the silver class are plotted in circles and squares, respectively.

only the 40 events in the gold class, the fraction of undulating events is $34-62\%$ (19/40, CL$=95\%$), and the fraction of strong undulations is $23-49\%$ (14/40). This suggests that the LC undulations are very common in the SLSN-I population.

Table 3. List of 24 undulating events

Strong		Weak
ZTF18aaisyyp ⋆	ZTF19abpbopt	ZTF18abshezu
ZTF18aajqcue	ZTF19acbonaa	ZTF18abszecm ⋆
ZTF18aapgrxo	ZTF19acgjpgh	ZTF18acapyww ⋆
ZTF18acyxnyw	ZTF19ackjrru	ZTF19aalbrph ⋆
ZTF19aamhhiz	ZTF20aadzbcf	ZTF19aaqrime
ZTF19aawfbtg	ZTF20aagikvv	ZTF19aarphwc
ZTF19abfvnns	ZTF20aaifybu	ZTF20aauoudz
ZTF19abnacvf	ZTF20abpuwxl ⋆	ZTF20abisijg

⋆ means the event in the silver sub-sample.

4.3. *Time scales and energetics of LC undulations*

From the RLCs, we can measure additional parameters, including phase, strength, time interval and energetics of each undulation. In this subsection, we focus on the 16 strongly undulating SLSNe-I, each of which may have multiple bumps/dips. We define the phase and the strength of each bump/dip by the time relative the peak phase and the amplitude of the RLC, Mag_{RLC}, when the RLC reaches the maximum/minimum, respectively. Counting only the significant undulations with the RLC SNR >3, we identify 36 undulations in the g band and 30 in the r band. This implies that on average, each undulating LC has roughly 2 significant bumps/dips.

Figure 13 presents the phase against the strength of the significant undulations, as well as their distributions. Bumps and dips each account for around half of the undulations. 73% of the undulations appear at post-peak phases and all the strong undulations (*e.g.* $|Mag_{RLC}| > 0.4$ mag) occur post peak. This indicates that pre-peak undulations are weaker and less common compared with post-peak ones, which is expected since the pre-peak LCs are usually much shorter than that of post-peak.

The next parameter is the time interval, Δt, which is defined as the time duration between two phases when their RLC values are zero (see Figure 9). The Δt in strongly undulating events have a wide range from 7 to 76 days, with a median value and 1σ error of $26.2^{+22.6}_{-10.7}$ days. For the central engine models (magnetar or black hole fallback, Kasen & Bildsten 2010; Dexter & Kasen 2013), the LC undulations could originate from the temporal change of the central source (see discussion in §5). However, any temporal variation from a central engine is smoothed by the photon diffusion in the expanding ejecta, and rapid variations would get washed out if the diffusion time is long.

Here Δt can be compared with t_{diff}^{eff}, the effective photon diffusion time scale, defined as

$$t_{diff}^{eff} = \left(\frac{2\kappa M_{ej}}{\beta c V_{ej}}\right)^{1/2}, \quad (1)$$

where β is a constant that equals 13.7, and κ, M_{ej} and V_{ej} are opacity, ejecta mass, and velocity, respectively. The instantaneous diffusion time scale, t_{diff}, can be calculated as $\left(t_{diff}^{eff}\right)^2/t$, where t is the phase relative to the explosion date taken from the `MOSFiT` modeling. After the peak, the ejecta gradually becomes transparent and the photospheric radius recedes inward. The instantaneous diffusion time of photons becomes shorter. The ratio of $\Delta t/t_{diff}^{eff}$ or $\Delta t/t_{diff}$ (approximately the δ in Hosseinzadeh et al. 2021) is a good indicator of whether the variable central engine scenario may drive the LC undulations. Specifically, if this ratio is less than 1, this model can not explain the undulations because of the smearing effect from the photon diffusion process.

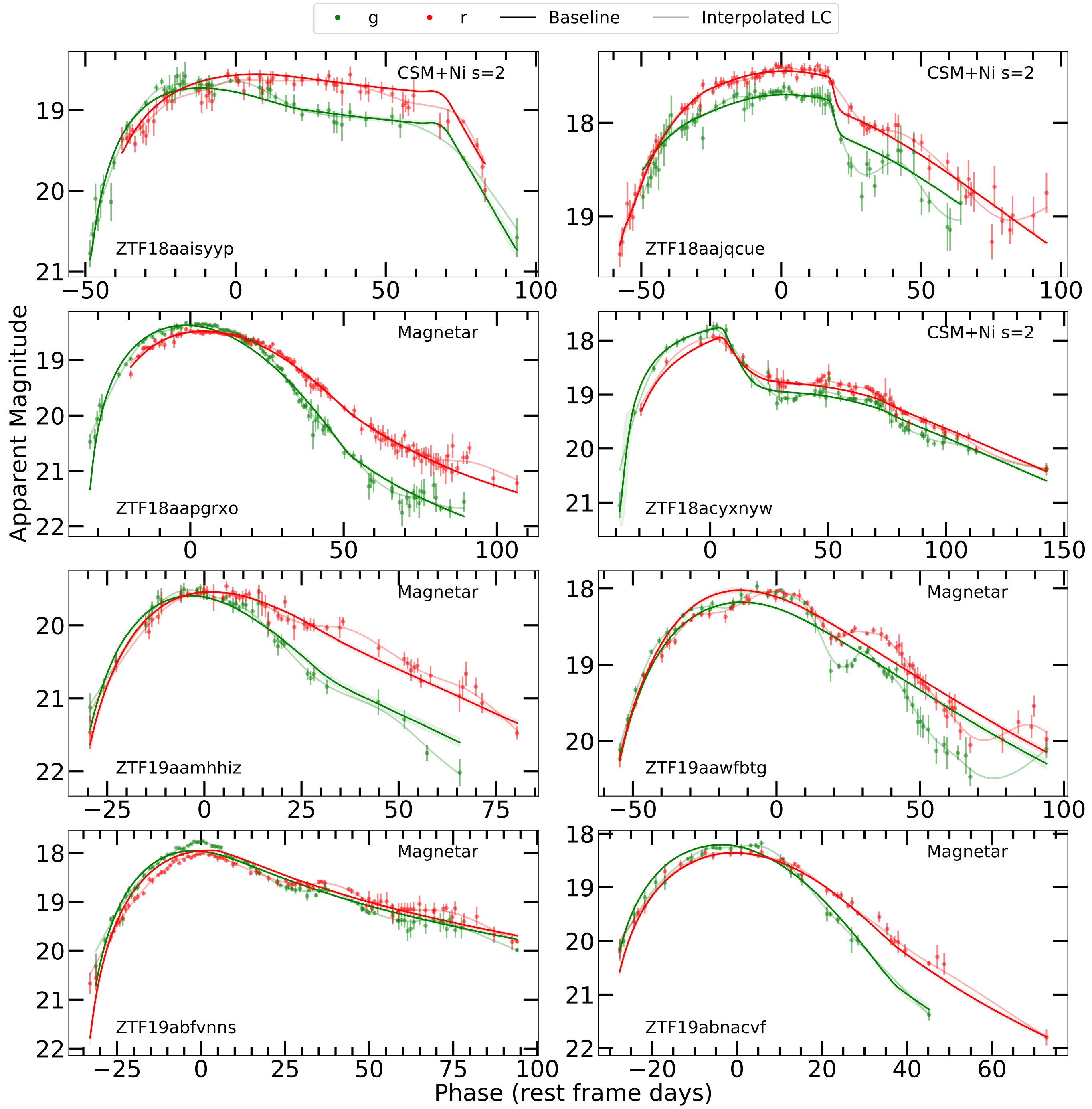

Figure 11. SLSN-I sample with strong undulations. Baseline models and GP interpolated LCs are plotted in solid lines and translucent lines respectively. The models of the baselines are labeled at the top right corner. The grey shaded area marks the data excluded from the fitting. (To be continued)

Of the 16 strongly undulating events, 12 are based on the magnetar model. Figure 14 displays their Δt versus the ratios of $\Delta t/t_{diff}^{eff}$ and $\Delta t/t_{diff}$. We find that 64% (30/47) of the undulations are shorter than t_{diff}^{eff} and 38% (18/47) are shorter than t_{diff}. 66% (8/12) and 58% (7/12) of the strongly undulating events have shorter undulations relative to either t_{diff}^{eff} or t_{diff}, respectively. Roughly half of the LC undulations (38−66%) have time intervals shorter than the photon diffusion time scales. This implies that emission variations of the central engine could be a viable explanation for about 50% of the undulations. For the other 50%, other physical processes are needed because the short time scale

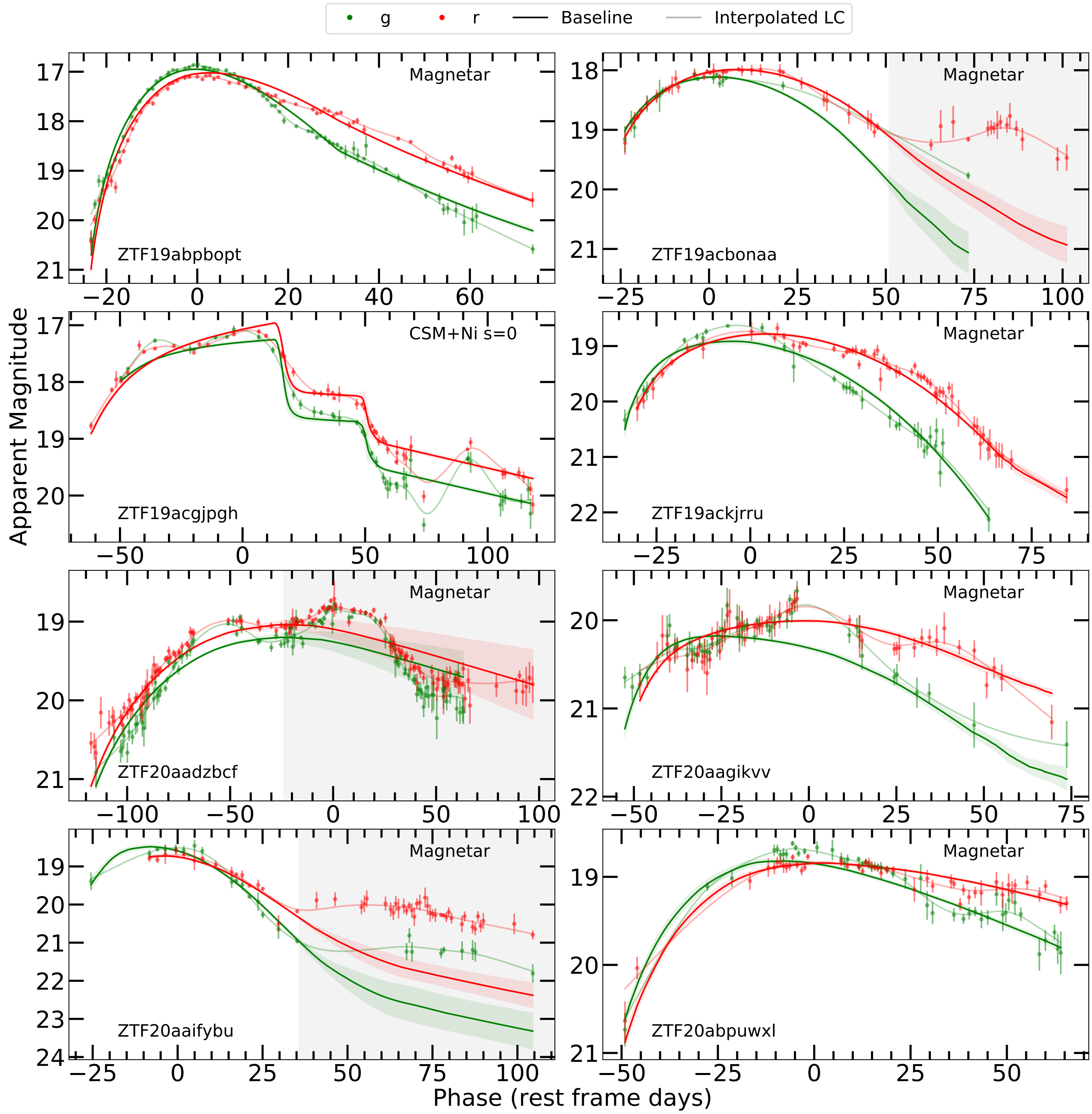

Figure 11. Continue.

undulations would get smoothed out by photon diffusion.

Finally, we measure the monochromatic energy of each significant undulation, $E_{\lambda,\mathrm{undu}}$, by integrating the flux differences between the LC and its baseline model (shown as the hatched area in Figure 9). We compute the ratio between $E_{\lambda,\mathrm{undu}}$ and the total monochromatic energy of the entire LC, $E_{\lambda,\mathrm{total}}$ for each undulation. Figure 15 plots the undulation energy versus the ratio. It is worth noting that most undulations appear to be quite energetic, with absolute values between 1.8×10^{47} to 3.6×10^{49} erg. However, they constitute only a small fraction of the total radiative energy, with the median energy ratio (absolute value) of $1.8\%^{+3.4\%}_{-0.9\%}$. The outliers in Figure 15 have very high energy ratios, and these SLSNe-I, *e.g.* ZTF19acbonaa and ZTF20aaifybu, have

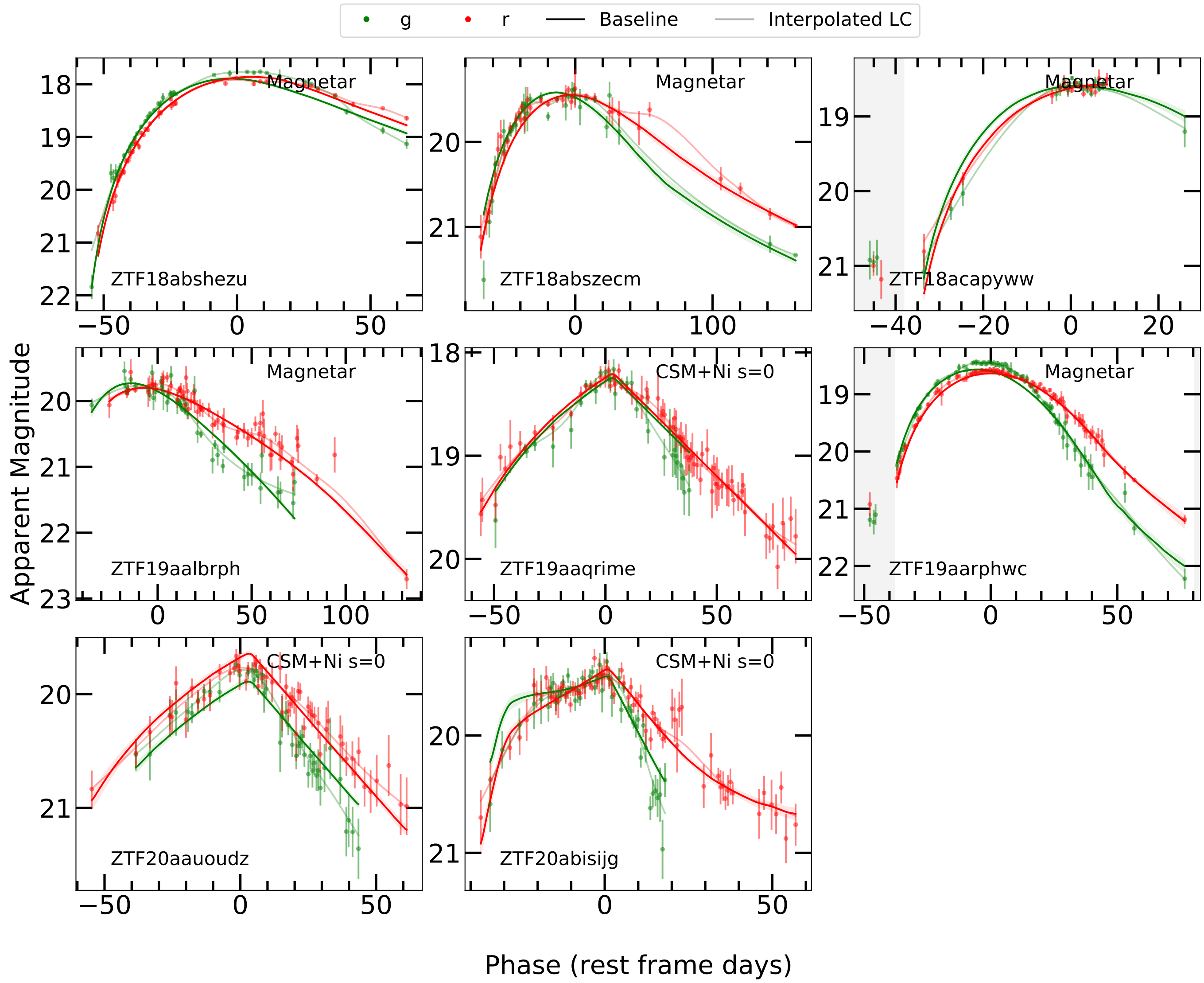

Figure 12. SLSN-I sample with weak undulations. Similar to Figure 11.

bright secondary peaks. The physical drivers powering these outliers may be different from the mechanisms working for the majority of the weaker undulations (see discussion below).

4.4. *Correlations*

The undulation properties may have intrinsic correlations which can reveal the possible physical mechanism. We test for correlations between the phases, absolute strengths, energies, time intervals of undulations and the half-maximum rise time timescales t_{rise} (the $t_{rise,1/2}$ from Paper I). Here the phase is relative to the explosion date determined by `MOSFiT`.

Hosseinzadeh et al. (2021) claimed that the phases of the bumps are moderately correlated with the LC rise times, implying that such bumps tend to happen at a certain evolutionary stage. However, observational selection effects play a significant role in their result because SLSNe-I with long rising time scales are also slow declining, and undulations are preferentially detected in slow fading events. It would be difficult to observe late time undulations in rapidly evolving events.

We carry out a simulation to quantify this observational bias. First we set $N = 10^4$ SLSN-I events with random t_{rise} from 10 to 85 days (approximate the range of our sample). Second we let the undulations **randomly** occur in a time range from explosion to a maximum detectable time t_{max}. The t_{max} usually highly correlates with the t_{rise} ($\rho = 0.64$, $p < 10^{-6}$ in our sample), since $t_{max} \approx t_{rise} + t_{decay}$ and it has been shown that slow-rising SLSNe-I tend to decay slow by different people (Paper I; Nicholl et al. 2015b; De Cia et al. 2018). The t_{max} is thus set random in a ±40-day-wide range along the empirical relation de-

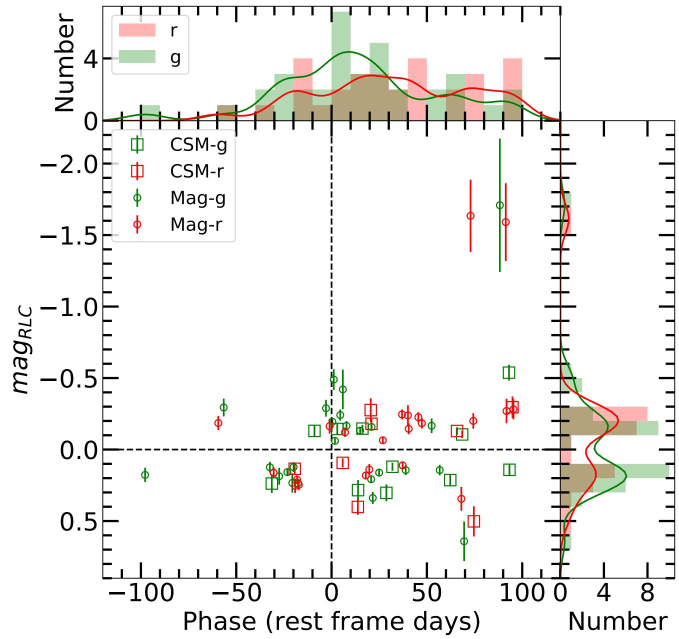

Figure 13. The phases versus the strengths of undulations. The strength is defined by the magnitude of the residual LC, Mag_{RLC}, where negative value means bumps. g- and r-band undulations are plotted in green and red, respectively. The CSM-favored events and the others using the magnetar baselines are marked with squares and dots, respectively. The vertical black dashed line marks the peak phase and the horizontal one marks the boundary between bumps and dips. The histograms along x and y axes show the distributions of the phase and the strength, respectively. The solid lines show the kernel density estimation of the distributions.

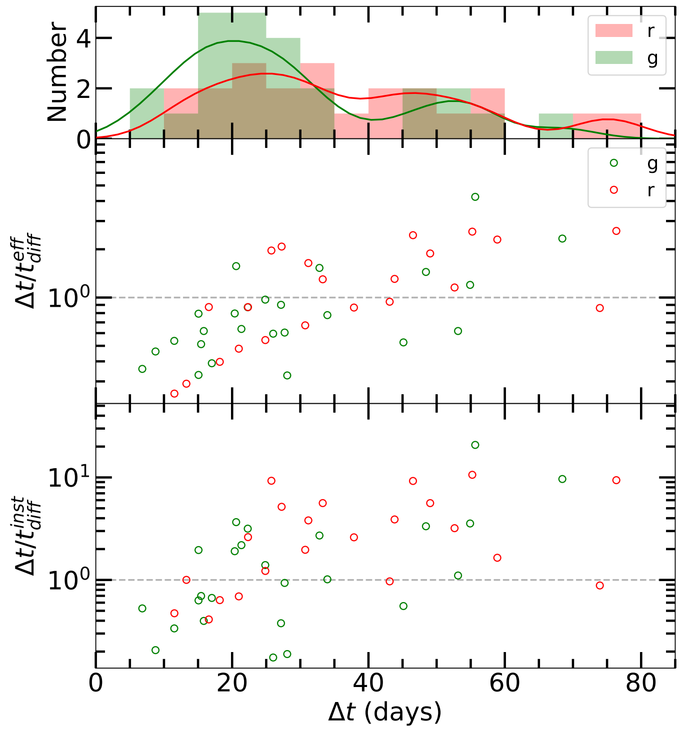

Figure 14. Time durations of the undulations, Δt, measured from the RLCs of the 12 strongly undulating events with the magnetar baselines. The top panel shows the distribution of Δt and the solid lines represent the kernel density estimations. The middle panel shows the ratio of Δt and the effective diffusion time scale t_{diff}^{eff}. The bottom panel shows the ratio of Δt and the instantaneous diffusion time scale t_{diff} at the corresponding undulation phase. The dashed horizontal lines mark $\Delta t = t_{diff}^{eff}$ and t_{diff}.

rived from our sample, $t_{max} \approx 2.5\ t_{rise} + 45$ days. As shown in Figure 16, the observational bias introduces a correlation ($\rho \approx 0.46,\ p < 10^{-7}$) between the undulation phases and the t_{rise}, which is comparable to the value ($\rho = 0.440,\ p < 10^{-3}$) measured with our real data. We further simulate a sample with Gaussian distributed t_{rise}, adjust the parameters and the random range of the empirical relation in a wide range from 50% to two times. This correlation always exists ($\rho = 0.27 - 0.51,\ p < 10^{-7}$). We conclude that the correlation between the undulation phase and the rise time is very likely due to observational selection effects and not a physical relation.

For other parameters, we only find weak positive correlation ($\rho = 0.377,\ p < 2\times10^{-3}$) between the phase and absolute strength as shown in Figure 17. If we exclude two special events (ZTF20aaifybu and ZTF19acbonaa) with an extremely strong and long-lived secondary peak, the correlation becomes weaker ($\rho = 0.313,\ p \approx 0.01$). The weak correlation may be biased because undulations at later phases are harder to detect among late time LCs

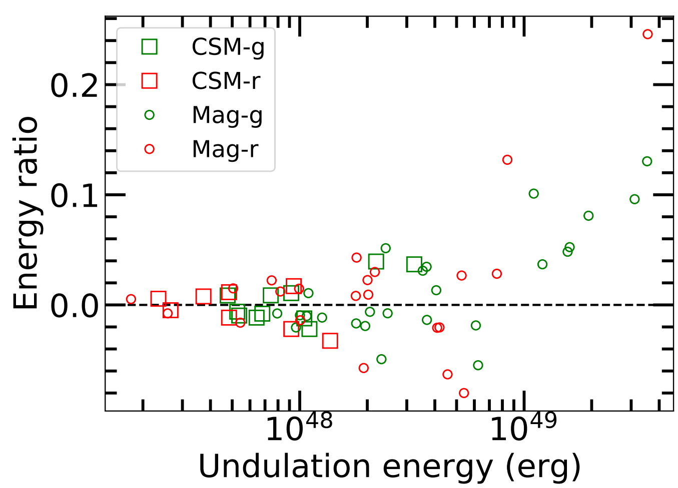

Figure 15. Energetics of the bumps/dips in the 16 strongly undulating events. X-axis is the integrated energy over the time interval of the undulation. Y-axis shows the ratio of undulation energy to the total radiative energy in g or r band over the entire LC.

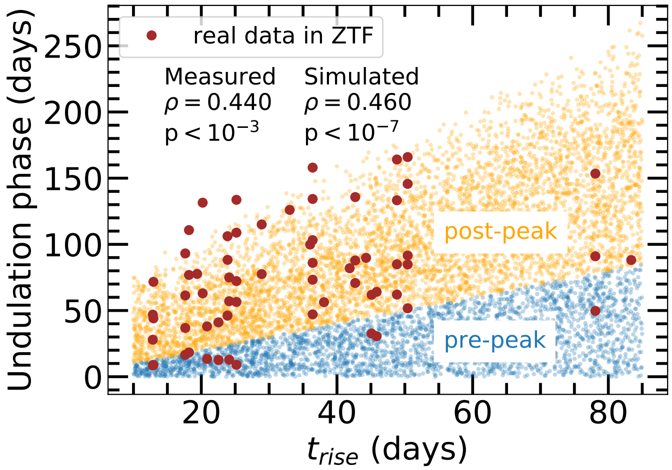

Figure 16. The observational selection effects on the rise time timescales and the undulation phases (relative to explosion). Pre- and post-peak simulated undulations are marked in blue and yellow, respectively. The measured data from our sample is presented with brown dots. By assuming undulations randomly occur in LCs, we find that observational effects will bring a moderate correlation ($\rho \approx 0.46,\ p < 10^{-7}$), which is comparable to the value measured in our sample ($\rho = 0.440,\ p < 10^{-3}$), illustrating that such a correlation could mainly be caused by an observational bias.

with low brightness and poorer sampling. Our data are not good enough to investigate this further.

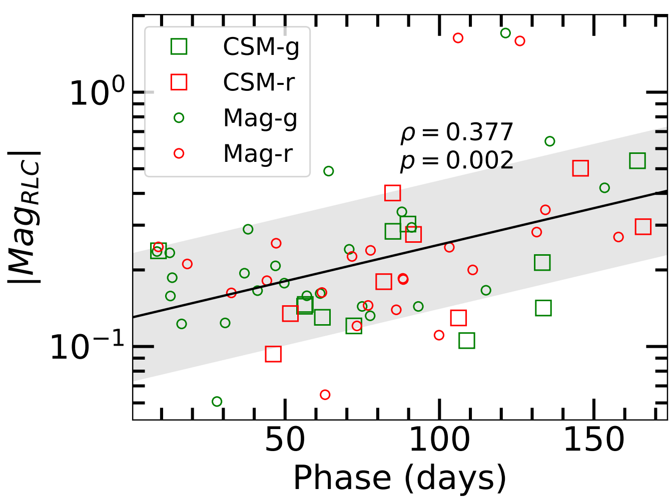

Figure 17. The correlation between the absolute strengths and time intervals of undulations. The correlation coefficient and the p-value are listed in the figure. The black solid line and the grey region show the result and 1σ error of the linear fit.

4.5. *Optical colors at bump phases*

The transient colors during the undulation phases could be an indicator of the physical processes. The observed $(g-r)$ colors of most of the undulations follow the general trend of the sample. However, six strongly undulating events stand out. In Figure 18, the blue lines are the observed $(g-r)$ color evolution tracks of six strongly undulating events. For comparison, the observed $(g-r)$ colors of the rest of the sample are shown in grey (see details in Paper I). Here we mark with the shaded vertical bars the period of times when the LC undulations are in excess, *i.e.* bump phases. These are quantitatively defined by the time intervals between the minima in the RLCs. From Figure 18, we note that during the bump phases, the observed $(g-r)$ colors are significantly bluer than that of the comparison sources. In particular, three events, ZTF18aajqcue, ZTF19aawfbtg and ZTF20abpuwxl, show much bluer colors when their LCs are varying, and turn redder again after or at the end of the bumps. The other three events, ZTF18acyxnyw, ZTF19abfvnns and ZTF19acgjpgh, are found to show much bluer and more stable colors than the general trend seen at late times ($> +40$ days). This result suggests that the CSM interaction could be an important energy source, and can naturally explain both the blue colors and the strong secondary peaks at late times for these six events. The duration of the blue color phase may be affected by the thickness of the CSM. However, magnetar heating can not be completely ruled out as different magnetar deposition profiles could also impact the color evolution at late times (Dessart 2019).

4.6. *LC undulations in Helium-rich SLSNe-Ib*

Yan et al. (2020) reported six He-rich SLSN-Ib events from the ZTF Phase-I SLSN-I sample. One additional event, ZTF20ablkuio, was thereafter spectroscopically classified as a SLSN-Ib by Terreran et al. (2020). Of these seven He-rich SLSNe-Ib, five events, namely ZTF18acyxnyw, ZTF19aamhhiz, ZTF19aawfbtg, ZTF19acgjpgh and ZTF20ablkuio, have gold LCs. Of these five SLSNe-Ib, four[2] have strong undulations, three[3] show much bluer color during their bump phases and three[4] strongly prefer the CSM+Ni model over the magnetar model, as shown in Figures 11, 18 and 4. All the five well-sampled He-rich SLSNe-Ib have either strongly undulating LCs or the LCs are much better fit by the CSM+Ni model. This small sample appears to have a much higher undulation fraction and a higher fraction of CMS+Ni powered LCs than those of the full sample.

[2] ZTF18acyxnyw, ZTF19acgjpgh, ZTF19aamhhiz and ZTF19aawfbtg

[3] ZTF18acyxnyw, ZTF19acgjpgh and ZTF19aawfbtg

[4] ZTF18acyxnyw, ZTF19acgjpgh and ZTF20ablkuio

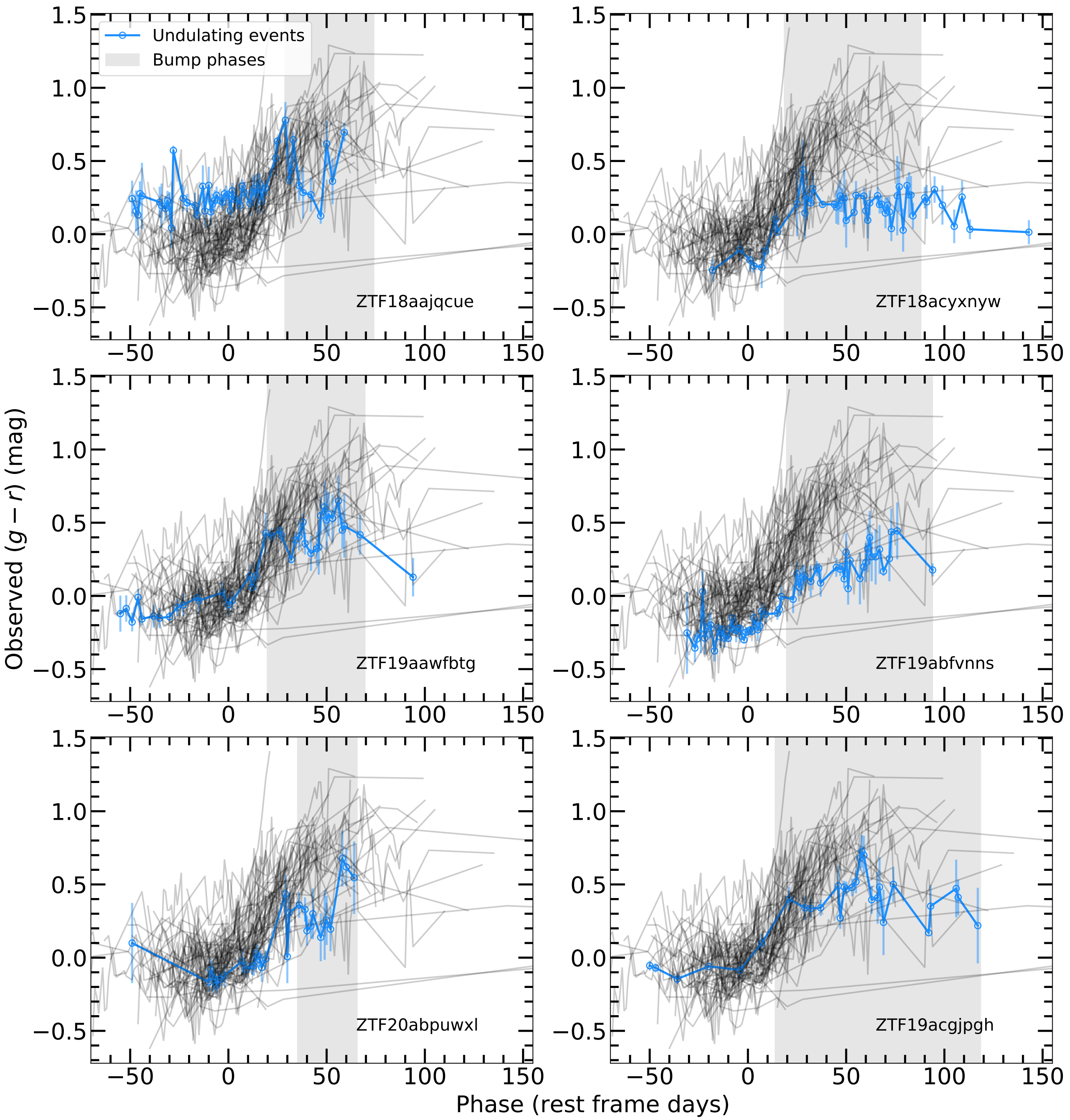

Figure 18. The observed $(g-r)$ colors as a function of rest-frame days relative to the peak phases. The blue tracks in the six panels are for the 6 strongly undulating events, overlaid on top of the color tracks of the full sample (gray lines). The bump phases are marked by the shaded vertical bars. All 6 panels show that the observed $g-r$ colors turn bluer during the bump phases.

These results suggest that CSM are present in He-rich SLSNe-Ib and leave significant imprints on their LCs. This is consistent with a scenario proposed in Yan et al. (2020), where the progenitors of SLSNe-Ib have lost most of their hydrogen envelopes but have not had enough time to also lose **all** of their helium layers. Because of the short time interval between the mass loss and the supernova explosion, it is likely that CSM are present near the progenitor stars. This scenario can naturally explain many of the observed characteristics of SLSNe-Ib, including He-rich spectra, LC undulations and blue colors during the bumps.

As for the remaining two of the seven SLSNe-Ib, ZTF19abrbsvm and ZTF19aauzyh, both have poorly sampled LCs. The absence of undulations in their LCs could simply be due to lack of data.

5. DISCUSSION

We modelled and analyzed the LCs of 70 gold and silver SLSN-I events presented in Paper I. Based on two commonly used SLSN models, the magnetar model and the CSM+Ni model, we explore the properties and possible mechanisms which drive LC undulations.

5.1. *What drives LC undulations among SLSNe-I?*

One major finding is that LC undulations are common, about $34-62\%$ of the SLSNe-I show such features. This fraction should be a lower limit as we count only undulations with strength SNR > 3 and some events are not well sampled at late times. This result is consistent with the fraction of $44-76\%$ found in Hosseinzadeh et al. (2021), which analysed the LC undulations based on a sample of 34 published SLSNe-I from multiple papers. Although the Hosseinzadeh et al. (2021) sample size is small, their LCs have good phase coverage out to +100 days post-peak. The undulation fraction for SLSNe-I is therefore quite high, and likely also higher than that of SNe Ic (Prentice et al. 2016; Lyman et al. 2016), although the actual undulation fraction for SNe Ic has not been measured and requires future work. For comparison, the undulation fraction for SNe IIn appears to be quite low, only $1.4^{+14.6}_{-1.0}\%$ from a study of 42 events from Palomar Transient Factory (Nyholm et al. 2020). This result has large uncertainties, and is therefore worth further validation with better LCs from ZTF.

The important question is what physical processes are driving the observed LC variations. There are two main possibilities. First, in the central engine scenario, the power output of the central source – either a magnetar or black hole fall-back accretion – may have a temporal variation. This intrinsic variation will be modulated (or smoothed) by photon diffusion in the ejecta. At a given phase, variations shorter than the photon diffusion time scales will be smoothed out and not observable at that phase. Figure 14 in §4.3 compares the undulation and photon diffusion time scales, illustrating that the central engine temporal variations could be a viable physical explanation for only 50% of the undulations. For the other 50%, which have shorter time scale undulations, different mechanisms are likely at work.

In the variable central engine scenario, as SNe evolve, the ejecta gradually becomes transparent. This implies that the LC undulations should be stronger and more easily to be observed at later times. Indeed, we find 73% of undulations and several strongest ones all occur post peak (§4.3). The variable central engine scenario could be supported by the observed weak correlation between the phase and absolute strength of undulations, discussed in §4.4

It is also possible that the central energy output is constant, but the ejecta opacity may undergo temporal changes, which in turn causes the variations in photospheric emission. This idea was proposed to explain the LC undulation in the luminous transient ASASSN-15lh (Margutti et al. 2017). If a central energy source can increase the ionization of the ejecta, this can lead to higher optical opacity due to electron scattering. Furthermore, the UV opacity, dominated by metal line transitions, can decrease as the ionized metal ions have fewer bound-bound transitions, leading to less opacity and higher UV emission. This may be the explanation for the extraordinarily UV bright, slowly evolving SLSN-I ZTF19acfwynw (see Paper I). In addition, when ejecta temperatures cool down, recombination of ionized ions can lead to reduction of optical opacity. If this opacity decrease occurs quickly, it can manifest itself as a LC undulation. Another important point about the magnetar driven model is that our current understanding is still limited and more detailed 3D hydrodynamic simulations are beginning to find interesting results, such as strong instabilities and mixing in a magnetar-powered SN with CSM (Chen et al. 2020).

The second mechanism is ejecta-CSM interaction. This process could be at work for at least ~50% of the SLSN-I undulations. CSI is an effective means to convert mechanical energy into thermal emission, and the CSM could have a variety of geometric and density distributions, *e.g.* shells or clumps. Vreeswijk et al. (2017); Liu et al. (2017a); Li et al. (2020) have applied the CSI model to explain the undulations observed in several SLSNe-I. The bluer $(g-r)$ colors during the undulating phases observed among some of our SLSNe-I provide evidence supporting the CSM model (see Figure 18). The simplistic picture is that the CSI can heat the ejecta and lead to both bluer colors and excess emission.

The LC shape under the CSI mechanism is highly dependent on the density profile of the CSM. The events with multiple peaks could have multiple CSM shells or clumpy CSM structures. One possible explanation is that the progenitor undergoes violent episodic mass losses (*e.g.* PPISN). The other is that the SLSN-I progenitor not only has an extended CSM due to significant mass loss prior to the explosion, but also has a binary companion which sweeps up and enhances the CSM density while orbiting the progenitor. This idea was proposed for the radio LC of SN 2001ig by Ryder et al. (2004).

Shock breakout has also been proposed to explain SLSN-I LC bumps at very early phases (so called double-peaked LCs). The energy source could be either magnetar/blackhole (Kasen et al. 2016) or CSM interaction (Moriya & Maeda 2012; Piro 2015). Some of the basic ideas may be viable for explaining the LC undulations at late times, such as changing of ionization states thus opacities. However, it is not clear how these models can work for undulations at post-peak phases. More quantitative modeling is needed.

Besides these two major models, there are other possible scenarios. For example, Kaplan & Soker (2020) suggests that the undulating LC of SN 2018don (ZTF18aajqcue; Lunnan et al. 2020) is the geometric effect of observing a different amount of emitting area from the two expanding photospheres of fast (polar) and slow (equatorial) outflows (or jets). The Kaplan & Soker (2020) study is based on the results from Quataert et al. (2019), which finds that the outer convection zones in yellow and red supergiants can generate enough angular momentum to form an accretion disk around the black hole. This model also predicts that these accretion flows could be highly time variable.

5.2. *Prevalence of H-poor CSM in SLSNe-I*

Of the 70 LCs, 14 have distinct features which are much better modelled by CSI with an assumed density profile (wind or constant). The fraction of SLSNe-I with H-poor CSM is between $33-53\%$, if we include events with undulations and smooth LCs preferentially fit by the CSI models.

This result has several implications for our understanding of the nature of SLSNe-I. First, if CSI plays an important role in driving undulations, such a high fraction implies that at the time of supernova explosion, H-poor CSM is likely present for a large fraction of SLSNe-I. This is the first time we have quantified how important CSI is for SLSNe-I using a carefully selected, large sample. Previously, many studies have preferred magnetar models for the SLSN-I population (Inserra et al. 2013; Nicholl et al. 2017b). One reason is its simplicity. Another indirect reason is lack of observational signatures of CSM interaction.

The presence of H-poor CSM around SLSNe-I also implies that the massive progenitor stars have not had enough time to completely disperse all of the outer envelopes before the core collapse happened. A fraction of these stars will have lost almost all their H-envelope but their He-rich outer layers are still present before the SN explosion. These events will appear as He-rich SLSNe-Ib (Yan et al. 2020). This also naturally explains why most of the SLSNe-Ib have undulating LCs which are better fit by the CSM+Ni model.

Furthermore, if the LC undulations could be explained by ejecta running into discrete CSM shells, this would imply that the progenitor mass loss is violent enough to eject large amounts of material. The CSM shell radius when the interaction occurs can be estimated by

$$R \approx V_{ej}\, t \tag{2}$$

where V_{ej} is the ejecta velocity output from `MOSFiT` and t is the phase of the undulation. For the strongly undulating events in our sample, the radii vary from 4×10^{14} to 1.5×10^{16} cm with a median value of 5.6×10^{15} cm. Assuming a stellar wind velocity of $10^2-10^3\,\mathrm{km\,s^{-1}}$, the CSM should be ejected several months to several decades before explosion.

6. SUMMARY

The three major results from our analysis are as follows.

1. LC undulations appear to be common, with $34-62\%$ of the sample showing significant departures from their smooth baseline LCs. Most of the undulations (73%) occur at post-peak phases. The energies within the undulations vary from 1.8×10^{47} to 3.6×10^{49} erg, usually $<20\%$ of the integrated radiative energy. The undulation time intervals and their observed $(g-r)$ colors suggest that both the CSI and the central engine with temporal variation are possible driving mechanisms. But the central engine variation can only explain about half of the undulations while the CSI can potentially work for all undulating events.

2. Our careful LC modeling finds that the majority of the sample (47/70=67%) can be equally well fit by both magnetar and CSM+Ni models. This implies that LCs alone can not unambiguously identify the power mechanism for SLSNe-I. The large

number of parameters in both of these models render some degeneracy which can not be broken by the LC data alone. However, a small fraction (14/70=20%) of LCs with specific features, such as inverted V-shape and steep LC decay, are clearly much better fit by the CSM+Ni model with either wind or constant density profiles. Only 9 out of 70 LCs prefer the magnetar model.

3. If LC undulations are indicators of CSI, our analysis and LC model fitting suggest that H-poor CSM is present in at least $33 - 53\%$ of the SLSN-I events. If the LCs with multiple undulations are interpreted as ejecta running into several CSM shells, this would imply that their massive progenitors experience violent, episodic mass loss events prior to the SN explosion. One such mechanism is PPISN, occurring in low-metallicity stars with ZAMS masses $> 70\, M_\odot$ (Woosley 2017).

We also summarize below additional statistical measurements from our sample.

1. We measure Fe II and O II velocities and estimate the photospheric velocities of SLSNe-I in our sample. SNe Ic-BL and normal SNe Ic show a strong negative correlation between the rise times and the photospheric velocities while the correlation becomes non-significant or weak when taking into account SLSNe-I. In general, SLSNe-I have moderate velocities between those of SNe Ic-BL and normal SNe Ic.

2. The fraction of SLSNe-I with early double-peak LCs is small, about $6-44\%$ (3/15) measured from a subset of LCs with early time data. This result is consistent with that of Angus et al. (2019) based on much deeper DES data. While this feature has previously been observed only in slow-evolving events, we observe a double-peak LC in a fast-evolving SLSN-I, ZTF19abpbopt.

3. For the 56 events which can be fit by the magnetar model, we find $P = 2.35^{+2.03}_{-0.72}$ ms, $B_\perp = 0.97^{+0.76}_{-0.67} \times 10^{14}$ G, $M_{ej} = 4.92^{+4.24}_{-2.19}\, M_\odot$ and $E_k = 2.41^{+2.08}_{-1.03} \times 10^{51}$ erg. We confirm the anti-correlation between M_{ej} and P found previously (Nicholl et al. 2017b; Blanchard et al. 2020; Hsu et al. 2021).

4. For the 47 events that can be fit equally well by both models, the final progenitor masses span over $6.36^{+4.80}_{-1.61}\, M_\odot$ and $20.52^{+27.04}_{-10.99}\, M_\odot$, estimated from the magnetar model and the CSM+Ni model respectively. The CSM+Ni model thus requires a much more massive progenitor.

In conclusion, our analysis of a large number of SLSN-I LCs has revealed and confirmed several important observational properties which only become obvious after the high cadence and well sampled ZTF LCs are available. Both LC shapes and the high fraction of undulations show clear indications that CSM may be present near many SLSN-I progenitors and play critical roles in their LC energetics and evolution. Intrinsic temporal variations of the central engine can also be a possible driver for LC undulations. Our papers (I & II) have put the studies of SLSN-I population on a solid statistical footing. The prospect for future progress lies with better modeling of the high quality ZTF LCs.

ACKNOWLEDGMENTS

We thank Dr. Weili Lin from Tsinghua University for useful discussions of CSM modeling of SLSN-I LCs. Based on observations obtained with the Samuel Oschin Telescope 48-inch and the 60-inch Telescope at the Palomar Observatory as part of the Zwicky Transient Facility project. ZTF is supported by the National Science Foundation under Grant No. AST-1440341 and a collaboration including Caltech, IPAC, the Weizmann Institute for Science, the Oskar Klein Center at Stockholm University, the University of Maryland, the University of Washington, Deutsches Elektronen-Synchrotron and Humboldt University, Los Alamos National Laboratories, the TANGO Consortium of Taiwan, the University of Wisconsin at Milwaukee, and Lawrence Berkeley National Laboratories. Operations are conducted by COO, IPAC, and UW. SED Machine is based upon work supported by the National Science Foundation under Grant No. 1106171. The ZTF forced-photometry service was funded under the Heising-Simons Foundation grant #12540303 (PI: Graham).

The Liverpool Telescope is operated on the island of La Palma by Liverpool John Moores University in the Spanish Observatorio del Roque de los Muchachos of the Instituto de Astrofisica de Canarias with financial support from the UK Science and Technology Facilities Council. The Nordic Optical Telescope is owned in collaboration by the University of Turku and Aarhus University, and operated jointly by Aarhus University, the University of Turku and the University of Oslo, representing Denmark, Finland and Norway, the University of Iceland and Stockholm University at the Observatorio del Roque de los Muchachos, La Palma, Spain, of the Instituto de Astrofisica de Canarias. This research has made use of data obtained through the High Energy Astrophysics Science Archive Research Center Online Service, provided by the NASA/Goddard Space Flight Center. This work was supported by the GROWTH project funded by the National Science Foundation under Grant No. 1545949.

S. S. acknowledges support from the G.R.E.A.T research environment, funded by *Vetenskapsrådet*, the Swedish Research Council, project number 2016-06012. T.-W. C. acknowledges the EU Funding under Marie Skłodowska-Curie grant H2020-MSCA-IF-2018-842471. T. K. acknowledges support from the Swedish National Space Agency and the Swedish Research Council. A. Gal-Yam acknowledges support from the EU via ERC grant No. 725161, the ISF GW excellence center, an IMOS space infrastructure grant and BSF/Transformative and GIF grants, as well as the André Deloro Institute for Advanced Research in Space and Optics, the Schwartz/Reisman Collaborative Science Program and the Norman E Alexander Family M Foundation ULTRASAT Data Center Fund, Minerva and Yeda-Sela. R. L. acknowledges support from a Marie Skłodowska-Curie Individual Fellowship within the Horizon 2020 European Union (EU) Framework Programme for Research and Innovation (H2020-MSCA-IF-2017-794467). The work of X. Wang is supported by the National Natural Science Foundation of China (NSFC grants 12033003 and 11633002), the Major State Basic Research Development Program (grant 2016YFA0400803), the Scholar Program of Beijing Academy of Science and Technology (DZ:BS202002), and the Tencent XPLORER Prize.

Software: `MOSFiT` (Guillochon et al. 2018) , `dynesty` (Speagle 2020).

APPENDIX

A. THE COMPLETE INFORMATION ON THE ZTF SLSN-I SAMPLE

Table A1. Spectral velocities.

Name	Phase (days)	Ion	Velocity ($\mathrm{km\,s^{-1}}$)
ZTF18aaisyyp	-4.53	Fe II	11080^{+440}_{-340}
ZTF18aajqcue	-2.18	Fe II	12370^{+500}_{-460}
ZTF18aajqcue	-1.25	Fe II	12500^{+660}_{-650}
ZTF18aajqcue	33.22	Fe II	4800^{+780}_{-550}
ZTF18aapgrxo	9.29	Fe II	17720^{+310}_{-310}
ZTF18aapgrxo	17.14	Fe II	15500^{+490}_{-650}
ZTF18aapgrxo	28.91	Fe II	14020^{+710}_{-670}
ZTF18aavrmcg	17.98	Fe II	16810^{+180}_{-220}
ZTF18aavrmcg	26.32	Fe II	12120^{+120}_{-130}

(This table is available in its entirety in machine-readable form.)

Table A2. Modeling parameters

Name	Magnetar					CSM					
	$B_\perp$ (10^{14}G)	P (ms)	M_{ej} ($M_\odot$)	V_{ej} ($10^4\,\mathrm{km\,s^{-1}}$)	χ^2/dof	s	$M_{\rm Ni}$ ($M_\odot$)	M_{CSM} ($M_\odot$)	M_{ej} ($M_\odot$)	V_{ej} ($10^4\,\mathrm{km\,s^{-1}}$)	χ^2/dof
ZTF18aaisyyp	$0.17^{+0.07}_{-0.05}$	$3.67^{+0.67}_{-0.62}$	$2.50^{+1.10}_{-0.61}$	$0.78^{+0.01}_{-0.00}$	3.75	2	$3.90^{+0.23}_{-0.21}$	$1.12^{+0.40}_{-0.31}$	$66.45^{+6.51}_{-7.13}$	$0.79^{+0.02}_{-0.01}$	2.30
ZTF18aajqcue	$0.51^{+0.14}_{-0.11}$	$5.56^{+0.75}_{-0.63}$	$8.87^{+0.73}_{-0.69}$	$0.88^{+0.01}_{-0.00}$	3.81	2	$5.81^{+0.67}_{-0.62}$	$0.14^{+0.04}_{-0.02}$	$20.64^{+2.58}_{-2.33}$	$1.25^{+0.05}_{-0.06}$	1.70
ZTF18aapgrxo	$1.19^{+0.26}_{-0.24}$	$1.82^{+0.19}_{-0.20}$	$9.06^{+1.11}_{-0.81}$	$1.06^{+0.02}_{-0.02}$	4.91	0	$3.69^{+0.22}_{-0.20}$	$4.85^{+0.45}_{-0.39}$	$29.51^{+2.15}_{-1.88}$	$1.03^{+0.02}_{-0.02}$	4.75
ZTF18aavrmcg	$3.02^{+0.59}_{-0.60}$	$2.52^{+0.59}_{-0.49}$	$1.47^{+0.52}_{-0.39}$	$1.09^{+0.05}_{-0.04}$	41.05	2	$0.10^{+0.13}_{-0.06}$	$0.53^{+0.12}_{-0.08}$	$17.22^{+8.36}_{-2.87}$	$1.55^{+0.03}_{-0.03}$	8.29
ZTF18aazgrfl	$0.71^{+0.21}_{-0.17}$	$1.04^{+0.28}_{-0.21}$	$24.31^{+8.94}_{-5.83}$	$0.90^{+0.12}_{-0.09}$	8.37	0	$0.58^{+0.82}_{-0.40}$	$14.09^{+7.35}_{-6.36}$	$42.41^{+31.61}_{-32.24}$	$1.10^{+0.16}_{-0.14}$	6.40
ZTF18abjwagv	$1.23^{+0.42}_{-0.32}$	$1.85^{+0.54}_{-0.60}$	$5.54^{+2.48}_{-1.38}$	$1.03^{+0.07}_{-0.06}$	2.47	2	$1.57^{+4.25}_{-1.30}$	$6.51^{+2.42}_{-1.72}$	$22.42^{+32.36}_{-15.71}$	$1.14^{+0.10}_{-0.07}$	2.47
ZTF18abmasep	$4.86^{+0.64}_{-0.93}$	$7.30^{+0.63}_{-0.87}$	$2.17^{+0.67}_{-0.57}$	$0.90^{+0.03}_{-0.03}$	4.57	0	$0.37^{+0.07}_{-0.03}$	$0.72^{+0.35}_{-0.16}$	$5.85^{+1.89}_{-2.08}$	$0.94^{+0.04}_{-0.05}$	6.66
ZTF18abshezu	$0.11^{+0.04}_{-0.03}$	$1.63^{+0.24}_{-0.24}$	$8.07^{+1.85}_{-1.37}$	$1.03^{+0.02}_{-0.03}$	44.82	2	$0.04^{+0.18}_{-0.03}$	$19.66^{+4.63}_{-3.23}$	$1.48^{+1.22}_{-0.77}$	$1.05^{+0.01}_{-0.01}$	81.21
ZTF18abszecm	$0.29^{+0.05}_{-0.06}$	$2.07^{+0.18}_{-0.22}$	$21.35^{+3.77}_{-3.50}$	$0.48^{+0.02}_{-0.02}$	3.73	2	$11.80^{+7.33}_{-7.96}$	$28.77^{+0.80}_{-1.38}$	$77.94^{+15.30}_{-24.30}$	$0.69^{+0.02}_{-0.02}$	6.74
ZTF18acapyww	$1.51^{+0.33}_{-0.34}$	$7.32^{+0.73}_{-1.08}$	$4.24^{+1.79}_{-1.17}$	$0.57^{+0.04}_{-0.04}$	3.04	0	$0.02^{+0.16}_{-0.02}$	$7.14^{+2.58}_{-1.69}$	$3.93^{+4.50}_{-2.60}$	$0.55^{+0.04}_{-0.03}$	2.47
ZTF18acqyvag	$1.42^{+0.25}_{-0.27}$	$4.33^{+0.50}_{-0.58}$	$1.73^{+0.63}_{-0.36}$	$1.15^{+0.08}_{-0.10}$	2.44	2	$3.82^{+0.41}_{-0.52}$	$3.35^{+0.90}_{-0.72}$	$20.69^{+10.56}_{-7.24}$	$1.25^{+0.08}_{-0.09}$	4.36
ZTF18acslpji	$0.36^{+0.05}_{-0.06}$	$2.63^{+0.18}_{-0.24}$	$4.80^{+0.72}_{-0.83}$	$0.81^{+0.02}_{-0.02}$	44.50	0	$2.92^{+0.58}_{-0.65}$	$12.67^{+2.07}_{-2.11}$	$40.47^{+8.77}_{-7.14}$	$0.98^{+0.02}_{-0.02}$	69.65
ZTF18acxgqxq	$1.20^{+0.22}_{-0.25}$	$1.72^{+0.29}_{-0.27}$	$8.53^{+3.62}_{-2.16}$	$0.84^{+0.07}_{-0.07}$	2.11	0	$3.34^{+0.33}_{-0.27}$	$6.07^{+3.21}_{-1.77}$	$56.17^{+17.02}_{-12.48}$	$0.90^{+0.08}_{-0.09}$	2.22
ZTF18acyxnyw	$1.15^{+0.22}_{-0.24}$	$8.51^{+0.78}_{-0.93}$	$1.79^{+1.04}_{-0.60}$	$0.61^{+0.05}_{-0.04}$	17.41	2	$2.37^{+0.07}_{-0.06}$	$2.01^{+0.15}_{-0.17}$	$10.39^{+0.75}_{-0.81}$	$0.57^{+0.01}_{-0.01}$	4.43
ZTF19aacxrab	$0.07^{+0.16}_{-0.04}$	$2.30^{+1.82}_{-0.91}$	$2.83^{+1.72}_{-0.88}$	$1.43^{+0.18}_{-0.09}$	14.69	2	$2.91^{+0.57}_{-0.47}$	$0.14^{+0.06}_{-0.03}$	$12.03^{+2.60}_{-2.08}$	$1.62^{+0.14}_{-0.12}$	2.62
ZTF19aajwogx	$1.03^{+0.33}_{-0.25}$	$1.65^{+0.60}_{-0.55}$	$8.99^{+5.06}_{-2.87}$	$0.79^{+0.08}_{-0.07}$	1.07	2	$0.27^{+0.89}_{-0.19}$	$10.91^{+4.47}_{-3.26}$	$17.74^{+33.20}_{-10.65}$	$0.93^{+0.10}_{-0.10}$	1.20
ZTF19aaknqmp	$5.40^{+1.32}_{-1.06}$	$1.69^{+0.46}_{-0.43}$	$7.24^{+2.63}_{-1.30}$	$1.21^{+0.04}_{-0.02}$	3.07	0	$0.03^{+0.11}_{-0.03}$	$1.34^{+0.50}_{-0.67}$	$1.74^{+4.28}_{-1.21}$	$1.22^{+0.05}_{-0.02}$	2.56
ZTF19aalbrph	$0.35^{+0.09}_{-0.06}$	$2.41^{+0.30}_{-0.23}$	$7.92^{+2.08}_{-2.27}$	$0.62^{+0.03}_{-0.03}$	2.11	0	$16.11^{+2.09}_{-3.29}$	$19.65^{+3.15}_{-3.20}$	$63.83^{+11.99}_{-9.22}$	$0.66^{+0.04}_{-0.03}$	2.49
ZTF19aamhast	$0.88^{+0.43}_{-0.26}$	$2.21^{+0.92}_{-0.74}$	$5.56^{+3.28}_{-2.34}$	$1.06^{+0.11}_{-0.09}$	1.71	0	$0.06^{+0.39}_{-0.04}$	$4.21^{+3.00}_{-1.39}$	$14.37^{+8.20}_{-11.17}$	$1.19^{+0.12}_{-0.09}$	1.79
ZTF19aamhhiz	$1.09^{+0.40}_{-0.44}$	$7.04^{+1.03}_{-0.94}$	$3.63^{+1.34}_{-1.21}$	$0.71^{+0.03}_{-0.04}$	2.25	2	$0.01^{+0.03}_{-0.01}$	$5.09^{+0.57}_{-0.53}$	$0.13^{+0.04}_{-0.02}$	$0.75^{+0.03}_{-0.03}$	2.13
ZTF19aanesgt	$1.75^{+0.71}_{-0.45}$	$2.34^{+1.37}_{-0.87}$	$3.61^{+1.62}_{-0.85}$	$1.38^{+0.10}_{-0.07}$	12.56	2	$0.21^{+2.26}_{-0.20}$	$3.15^{+1.08}_{-0.55}$	$2.26^{+18.69}_{-2.07}$	$1.46^{+0.12}_{-0.10}$	7.92
ZTF19aantokv	$1.13^{+0.36}_{-0.42}$	$1.71^{+0.75}_{-0.45}$	$11.64^{+3.74}_{-4.61}$	$0.95^{+0.06}_{-0.06}$	1.60	0	$0.16^{+0.34}_{-0.10}$	$10.28^{+3.32}_{-4.60}$	$17.76^{+24.18}_{-12.07}$	$1.02^{+0.03}_{-0.07}$	1.56
ZTF19aaohuwc	$1.02^{+0.31}_{-0.33}$	$4.09^{+0.59}_{-0.59}$	$3.68^{+1.64}_{-1.08}$	$0.75^{+0.04}_{-0.03}$	3.56	0	$0.17^{+0.50}_{-0.12}$	$2.94^{+4.06}_{-1.13}$	$31.94^{+16.55}_{-20.00}$	$0.79^{+0.06}_{-0.05}$	3.53
ZTF19aapaeye	$0.81^{+0.12}_{-0.16}$	$4.96^{+0.35}_{-0.53}$	$1.37^{+0.44}_{-0.29}$	$1.17^{+0.04}_{-0.04}$	2.00	0	$0.02^{+0.22}_{-0.02}$	$3.85^{+1.51}_{-0.87}$	$1.34^{+1.69}_{-0.84}$	$1.29^{+0.05}_{-0.05}$	2.01

Table A2 *continued*

Table A2 *(continued)*

Name	Magnetar					CSM					
	$B_\perp$ (10^{14}G)	P (ms)	M_{ej} ($M_\odot$)	V_{ej} (10^4 km s^{-1})	χ^2/dof	s	$M_{\rm Ni}$ ($M_\odot$)	M_{CSM} ($M_\odot$)	M_{ej} ($M_\odot$)	V_{ej} (10^4 km s^{-1})	χ^2/dof
ZTF19aaqrime	$0.04^{+0.01}_{-0.01}$	$1.14^{+0.16}_{-0.17}$	$13.64^{+2.90}_{-2.37}$	$1.27^{+0.01}_{-0.01}$	3.72	0	$0.00^{+0.03}_{-0.00}$	$18.24^{+2.23}_{-1.46}$	$0.17^{+0.09}_{-0.05}$	$1.34^{+0.06}_{-0.05}$	1.14
ZTF19aarphwc	$0.73^{+0.24}_{-0.16}$	$2.07^{+0.32}_{-0.36}$	$8.91^{+2.00}_{-1.36}$	$1.00^{+0.04}_{-0.03}$	10.69	0	$0.19^{+0.52}_{-0.14}$	$4.51^{+0.46}_{-0.41}$	$27.73^{+2.44}_{-1.99}$	$1.10^{+0.02}_{-0.02}$	22.48
ZTF19aaruixj	$0.99^{+0.28}_{-0.31}$	$2.36^{+0.34}_{-0.48}$	$3.44^{+1.31}_{-0.95}$	$0.97^{+0.01}_{-0.02}$	0.63	0	$0.26^{+1.56}_{-0.21}$	$13.19^{+3.68}_{-2.81}$	$19.00^{+9.93}_{-6.99}$	$0.98^{+0.01}_{-0.02}$	0.77
ZTF19aasdvfr	$0.96^{+2.17}_{-0.27}$	$4.07^{+0.61}_{-3.00}$	$2.78^{+15.95}_{-0.66}$	$1.11^{+0.15}_{-0.08}$	0.67	0	$0.07^{+0.15}_{-0.05}$	$4.27^{+2.68}_{-1.10}$	$3.75^{+4.77}_{-2.61}$	$1.20^{+0.17}_{-0.12}$	0.68
ZTF19aauiref	$0.72^{+0.28}_{-0.25}$	$1.27^{+0.48}_{-0.37}$	$6.81^{+3.09}_{-2.11}$	$1.06^{+0.07}_{-0.09}$	2.71	2	$2.47^{+11.07}_{-2.22}$	$26.92^{+1.95}_{-3.02}$	$74.45^{+15.78}_{-20.41}$	$1.15^{+0.01}_{-0.02}$	4.74
ZTF19aauvzyh	$0.04^{+0.07}_{-0.02}$	$2.16^{+1.34}_{-0.66}$	$4.41^{+2.09}_{-1.45}$	$1.14^{+0.28}_{-0.11}$	3.52	2	$0.03^{+0.28}_{-0.03}$	$14.26^{+4.97}_{-5.75}$	$1.11^{+11.64}_{-0.89}$	$1.07^{+0.12}_{-0.06}$	3.78
ZTF19aavouyw	$3.51^{+0.93}_{-0.76}$	$2.90^{+1.11}_{-0.91}$	$3.83^{+1.58}_{-0.90}$	$1.02^{+0.01}_{-0.01}$	8.46	2	$0.03^{+0.06}_{-0.03}$	$2.33^{+0.41}_{-0.37}$	$0.27^{+0.26}_{-0.12}$	$1.17^{+0.10}_{-0.08}$	9.51
ZTF19aawfbtg	$0.85^{+0.27}_{-0.23}$	$7.36^{+0.85}_{-0.91}$	$6.66^{+0.80}_{-0.73}$	$0.78^{+0.01}_{-0.01}$	14.06	2	$3.48^{+0.19}_{-0.20}$	$0.15^{+0.05}_{-0.03}$	$9.04^{+1.52}_{-1.04}$	$0.81^{+0.06}_{-0.03}$	11.24
ZTF19aawsqsc	$1.92^{+0.35}_{-0.38}$	$4.59^{+0.51}_{-0.51}$	$3.40^{+0.61}_{-0.46}$	$0.95^{+0.04}_{-0.04}$	1.65	0	$1.85^{+0.19}_{-0.18}$	$2.12^{+0.29}_{-0.19}$	$9.11^{+1.08}_{-0.71}$	$0.90^{+0.03}_{-0.03}$	1.40
ZTF19aayclnm	$0.09^{+0.05}_{-0.03}$	$1.55^{+0.35}_{-0.27}$	$10.46^{+3.38}_{-2.63}$	$1.02^{+0.03}_{-0.01}$	2.75	2	$0.07^{+0.22}_{-0.06}$	$17.74^{+5.57}_{-3.35}$	$1.38^{+2.11}_{-0.89}$	$1.02^{+0.02}_{-0.01}$	2.39
ZTF19abaeyqw	$0.43^{+0.28}_{-0.13}$	$2.35^{+0.32}_{-0.34}$	$5.63^{+1.78}_{-1.10}$	$0.99^{+0.04}_{-0.04}$	0.84	2	$0.02^{+0.12}_{-0.02}$	$12.91^{+4.03}_{-2.85}$	$0.84^{+1.85}_{-0.55}$	$1.28^{+0.08}_{-0.07}$	1.51
ZTF19abcvwrz	$0.93^{+0.34}_{-0.25}$	$2.16^{+0.87}_{-0.65}$	$11.59^{+4.56}_{-3.36}$	$0.80^{+0.05}_{-0.05}$	0.88	2	$0.04^{+0.29}_{-0.03}$	$11.19^{+2.27}_{-1.30}$	$4.42^{+5.66}_{-2.54}$	$0.81^{+0.04}_{-0.04}$	0.56
ZTF19abdlzyq	$1.23^{+0.47}_{-0.38}$	$3.76^{+0.88}_{-1.07}$	$2.62^{+0.72}_{-0.63}$	$1.19^{+0.06}_{-0.08}$	0.87	0	$0.01^{+0.12}_{-0.01}$	$4.27^{+3.38}_{-1.78}$	$1.38^{+4.65}_{-1.11}$	$1.21^{+0.05}_{-0.07}$	0.71
ZTF19abfvnns	$0.98^{+0.19}_{-0.20}$	$5.94^{+0.56}_{-0.64}$	$2.92^{+0.45}_{-0.34}$	$1.00^{+0.01}_{-0.00}$	19.11	2	$0.00^{+0.01}_{-0.00}$	$5.57^{+0.25}_{-0.29}$	$0.12^{+0.03}_{-0.02}$	$1.01^{+0.01}_{-0.00}$	17.95
ZTF19abnacvf	$1.48^{+0.28}_{-0.30}$	$3.75^{+0.40}_{-0.42}$	$3.72^{+0.51}_{-0.39}$	$0.92^{+0.03}_{-0.03}$	4.58	2	$0.70^{+0.15}_{-0.13}$	$4.12^{+0.78}_{-0.58}$	$10.44^{+7.61}_{-5.96}$	$0.96^{+0.03}_{-0.03}$	3.37
ZTF19abnqqdp	$1.13^{+0.24}_{-0.24}$	$2.49^{+0.41}_{-0.42}$	$3.76^{+1.12}_{-0.77}$	$1.19^{+0.08}_{-0.09}$	1.24	2	$12.88^{+8.09}_{-4.62}$	$4.50^{+1.80}_{-0.66}$	$39.26^{+25.74}_{-15.41}$	$1.18^{+0.09}_{-0.08}$	0.86
ZTF19abpbopt	$0.37^{+0.09}_{-0.08}$	$3.52^{+0.41}_{-0.38}$	$2.24^{+0.29}_{-0.24}$	$1.47^{+0.01}_{-0.00}$	34.02	0	$0.01^{+0.05}_{-0.01}$	$2.91^{+0.28}_{-0.25}$	$0.19^{+0.06}_{-0.05}$	$1.48^{+0.02}_{-0.01}$	27.51
ZTF19abuyuwa	$1.03^{+0.19}_{-0.31}$	$0.92^{+0.27}_{-0.15}$	$22.50^{+8.70}_{-7.75}$	$0.98^{+0.03}_{-0.02}$	1.25	2	$0.25^{+2.30}_{-0.21}$	$15.60^{+6.75}_{-5.49}$	$20.82^{+30.60}_{-13.95}$	$1.08^{+0.08}_{-0.06}$	1.18
ZTF19abzoyeg	$2.52^{+0.91}_{-0.65}$	$1.73^{+0.87}_{-0.77}$	$3.47^{+1.49}_{-0.45}$	$0.61^{+0.01}_{-0.01}$	2.00	0	$0.12^{+0.13}_{-0.05}$	$6.38^{+1.26}_{-0.83}$	$46.43^{+8.08}_{-8.78}$	$0.60^{+0.01}_{-0.01}$	1.75
ZTF19abzqmau	$1.78^{+0.38}_{-0.35}$	$1.63^{+1.21}_{-0.55}$	$3.97^{+1.23}_{-1.28}$	$0.95^{+0.08}_{-0.06}$	1.67	0	$0.14^{+0.40}_{-0.11}$	$3.44^{+1.34}_{-0.94}$	$6.52^{+2.66}_{-2.81}$	$1.11^{+0.04}_{-0.05}$	1.89
ZTF19acbonaa	$1.51^{+0.40}_{-0.33}$	$1.56^{+0.88}_{-0.57}$	$8.69^{+3.26}_{-2.01}$	$0.80^{+0.04}_{-0.05}$	0.79	0	$0.94^{+1.27}_{-0.64}$	$6.33^{+6.44}_{-1.94}$	$31.42^{+30.07}_{-7.94}$	$0.72^{+0.06}_{-0.07}$	0.69
ZTF19acfwynw	$0.64^{+0.17}_{-0.14}$	$1.83^{+0.44}_{-0.45}$	$34.68^{+17.75}_{-9.38}$	$0.41^{+0.04}_{-0.03}$	13.30	2	$1.01^{+1.99}_{-0.88}$	$25.80^{+2.37}_{-2.51}$	$20.25^{+19.01}_{-8.26}$	$0.60^{+0.03}_{-0.04}$	13.79
ZTF19acgjpgh	$0.49^{+0.20}_{-0.16}$	$6.12^{+1.03}_{-1.04}$	$3.09^{+0.85}_{-0.80}$	$1.04^{+0.04}_{-0.02}$	199.69	0	$1.27^{+0.12}_{-0.10}$	$1.79^{+0.26}_{-0.16}$	$2.60^{+0.24}_{-0.20}$	$1.02^{+0.01}_{-0.00}$	56.89
ZTF19ackjrru	$0.44^{+0.14}_{-0.11}$	$4.25^{+0.61}_{-0.49}$	$2.35^{+0.47}_{-0.42}$	$1.16^{+0.04}_{-0.03}$	5.92	2	$0.00^{+0.01}_{-0.00}$	$6.33^{+0.80}_{-0.70}$	$1.98^{+2.40}_{-1.37}$	$1.18^{+0.05}_{-0.04}$	4.44
ZTF19acsajxn	$1.24^{+0.26}_{-0.49}$	$1.75^{+2.91}_{-0.56}$	$9.58^{+3.25}_{-5.57}$	$0.82^{+0.06}_{-0.07}$	1.16	0	$0.24^{+1.24}_{-0.14}$	$5.70^{+0.95}_{-2.11}$	$2.66^{+4.72}_{-1.28}$	$0.71^{+0.05}_{-0.04}$	0.86
ZTF19acujvsi	$0.61^{+0.21}_{-0.15}$	$4.99^{+0.44}_{-0.78}$	$5.16^{+2.08}_{-1.37}$	$0.65^{+0.06}_{-0.05}$	1.38	0	$0.15^{+0.58}_{-0.14}$	$16.58^{+6.56}_{-4.94}$	$2.47^{+4.81}_{-1.56}$	$0.65^{+0.05}_{-0.05}$	1.19
ZTF19adaivcf	$0.57^{+0.16}_{-0.15}$	$2.19^{+0.34}_{-0.36}$	$6.90^{+1.36}_{-1.89}$	$0.90^{+0.01}_{-0.02}$	0.87	0	$0.54^{+4.68}_{-0.46}$	$13.33^{+3.89}_{-2.17}$	$29.51^{+4.73}_{-11.94}$	$0.85^{+0.03}_{-0.03}$	0.92
ZTF20aadzbcf	$0.03^{+0.01}_{-0.01}$	$1.18^{+0.25}_{-0.19}$	$28.75^{+6.28}_{-5.06}$	$0.88^{+0.12}_{-0.08}$	5.78	0	$0.01^{+0.09}_{-0.01}$	$26.07^{+2.38}_{-3.04}$	$0.70^{+0.92}_{-0.46}$	$0.87^{+0.11}_{-0.08}$	4.16
ZTF20aagikvv	$0.04^{+0.02}_{-0.01}$	$1.40^{+0.27}_{-0.18}$	$2.03^{+0.20}_{-0.14}$	$0.87^{+0.01}_{-0.00}$	3.67	2	$0.11^{+0.57}_{-0.08}$	$10.64^{+2.82}_{-2.68}$	$7.68^{+9.78}_{-4.17}$	$0.87^{+0.01}_{-0.00}$	3.11
ZTF20aahbfmf	$1.92^{+0.46}_{-0.39}$	$2.46^{+0.48}_{-0.43}$	$4.01^{+0.88}_{-0.71}$	$1.26^{+0.03}_{-0.02}$	3.17	0	$0.21^{+0.24}_{-0.12}$	$2.71^{+1.44}_{-0.96}$	$9.46^{+4.30}_{-5.55}$	$1.27^{+0.06}_{-0.03}$	3.83
ZTF20aahrxgw	$1.66^{+0.39}_{-0.38}$	$3.73^{+0.58}_{-0.76}$	$2.74^{+1.04}_{-0.66}$	$1.01^{+0.07}_{-0.07}$	1.55	2	$0.79^{+1.84}_{-0.75}$	$3.93^{+1.02}_{-0.86}$	$9.02^{+22.11}_{-6.28}$	$1.05^{+0.16}_{-0.09}$	1.71
ZTF20aaifybu	$1.73^{+0.36}_{-0.40}$	$1.83^{+0.49}_{-0.37}$	$4.48^{+2.46}_{-1.13}$	$0.94^{+0.03}_{-0.04}$	3.40	2	$1.58^{+2.29}_{-1.39}$	$7.68^{+2.15}_{-1.38}$	$60.27^{+22.69}_{-22.27}$	$0.84^{+0.06}_{-0.06}$	3.13
ZTF20aaoqwpo	$0.14^{+0.03}_{-0.03}$	$1.50^{+0.18}_{-0.18}$	$6.88^{+0.84}_{-0.91}$	$1.49^{+0.02}_{-0.01}$	7.42	2	$0.02^{+0.16}_{-0.02}$	$9.28^{+1.63}_{-1.12}$	$2.57^{+4.67}_{-1.29}$	$1.50^{+0.03}_{-0.01}$	3.96
ZTF20aapaecd	$1.85^{+0.39}_{-0.33}$	$3.26^{+1.17}_{-1.13}$	$20.99^{+8.23}_{-4.51}$	$0.43^{+0.02}_{-0.02}$	1.54	0	$0.13^{+0.19}_{-0.07}$	$7.13^{+1.09}_{-1.29}$	$40.42^{+7.38}_{-3.84}$	$0.38^{+0.01}_{-0.01}$	1.44
ZTF20aattyuz	$3.88^{+0.77}_{-0.72}$	$6.64^{+0.75}_{-0.75}$	$2.15^{+0.85}_{-0.60}$	$0.67^{+0.02}_{-0.02}$	2.07	2	$0.34^{+0.11}_{-0.31}$	$1.84^{+0.79}_{-0.94}$	$21.80^{+5.48}_{-9.68}$	$0.73^{+0.10}_{-0.15}$	3.29
ZTF20aauoudz	$0.06^{+0.02}_{-0.02}$	$1.60^{+0.28}_{-0.25}$	$9.84^{+1.51}_{-1.57}$	$1.21^{+0.08}_{-0.04}$	4.87	0	$0.00^{+0.02}_{-0.00}$	$11.72^{+0.75}_{-0.61}$	$0.13^{+0.03}_{-0.02}$	$1.19^{+0.03}_{-0.02}$	1.64
ZTF20aavfbqz	$0.39^{+0.15}_{-0.11}$	$3.08^{+0.34}_{-0.34}$	$2.92^{+1.32}_{-0.80}$	$0.98^{+0.07}_{-0.05}$	1.31	0	$0.20^{+0.69}_{-0.17}$	$13.42^{+5.37}_{-9.02}$	$9.07^{+20.81}_{-5.27}$	$0.97^{+0.14}_{-0.06}$	1.39
ZTF20aavqrzc	$0.16^{+0.05}_{-0.04}$	$2.26^{+0.28}_{-0.27}$	$3.31^{+1.08}_{-0.71}$	$1.08^{+0.11}_{-0.06}$	3.97	0	$0.20^{+1.10}_{-0.17}$	$21.15^{+4.92}_{-6.09}$	$10.86^{+14.60}_{-6.77}$	$1.11^{+0.15}_{-0.08}$	4.81
ZTF20aawfxlt	$0.96^{+0.23}_{-0.19}$	$2.71^{+0.34}_{-0.31}$	$5.05^{+0.97}_{-0.76}$	$0.99^{+0.04}_{-0.04}$	1.69	2	$4.11^{+4.99}_{-3.90}$	$7.16^{+2.90}_{-1.71}$	$11.61^{+12.41}_{-9.48}$	$1.01^{+0.06}_{-0.06}$	1.56
ZTF20aawkgxa	$0.04^{+0.02}_{-0.01}$	$1.26^{+0.21}_{-0.16}$	$2.72^{+0.36}_{-0.26}$	$1.00^{+0.02}_{-0.01}$	1.12	2	$13.86^{+2.90}_{-1.94}$	$11.57^{+4.62}_{-2.13}$	$52.16^{+20.93}_{-16.22}$	$1.11^{+0.04}_{-0.04}$	1.29
ZTF20abisijg	$0.67^{+0.15}_{-0.13}$	$3.39^{+0.40}_{-0.36}$	$4.52^{+0.79}_{-0.63}$	$0.91^{+0.05}_{-0.05}$	2.45	0	$14.93^{+1.90}_{-1.57}$	$3.37^{+1.55}_{-0.95}$	$34.36^{+10.84}_{-5.07}$	$0.98^{+0.04}_{-0.04}$	1.56
ZTF20abjwjrx	$0.44^{+0.13}_{-0.11}$	$4.17^{+0.49}_{-0.51}$	$5.30^{+0.71}_{-0.68}$	$0.96^{+0.02}_{-0.01}$	6.21	2	$0.02^{+0.14}_{-0.02}$	$10.32^{+3.01}_{-1.99}$	$0.92^{+2.03}_{-0.59}$	$0.97^{+0.03}_{-0.02}$	5.39
ZTF20ablkuio	$1.03^{+0.21}_{-0.21}$	$8.00^{+0.77}_{-0.87}$	$2.84^{+1.20}_{-0.72}$	$0.68^{+0.04}_{-0.03}$	4.39	2	$3.83^{+0.22}_{-0.21}$	$2.56^{+0.37}_{-0.35}$	$12.22^{+2.12}_{-1.73}$	$0.65^{+0.02}_{-0.02}$	0.89
ZTF20abpuwxl	$0.30^{+0.06}_{-0.06}$	$3.00^{+0.27}_{-0.32}$	$5.73^{+2.35}_{-1.33}$	$0.65^{+0.03}_{-0.03}$	4.59	2	$4.30^{+10.81}_{-4.07}$	$14.61^{+5.81}_{-4.59}$	$21.86^{+21.80}_{-12.39}$	$0.71^{+0.01}_{-0.01}$	6.39
ZTF20abzaacf	$0.07^{+0.02}_{-0.01}$	$2.33^{+0.36}_{-0.26}$	$8.71^{+1.27}_{-0.98}$	$0.91^{+0.04}_{-0.03}$	1.37	2	$8.19^{+0.37}_{-0.39}$	$1.41^{+8.44}_{-1.16}$	$44.82^{+15.34}_{-11.98}$	$1.04^{+0.05}_{-0.05}$	1.52
ZTF20aceqspy	$1.32^{+0.45}_{-0.38}$	$2.66^{+0.65}_{-0.71}$	$4.18^{+1.50}_{-0.95}$	$1.10^{+0.07}_{-0.07}$	1.39	0	$0.64^{+3.35}_{-0.52}$	$2.40^{+0.82}_{-0.50}$	$21.14^{+7.14}_{-4.01}$	$1.27^{+0.08}_{-0.08}$	1.12

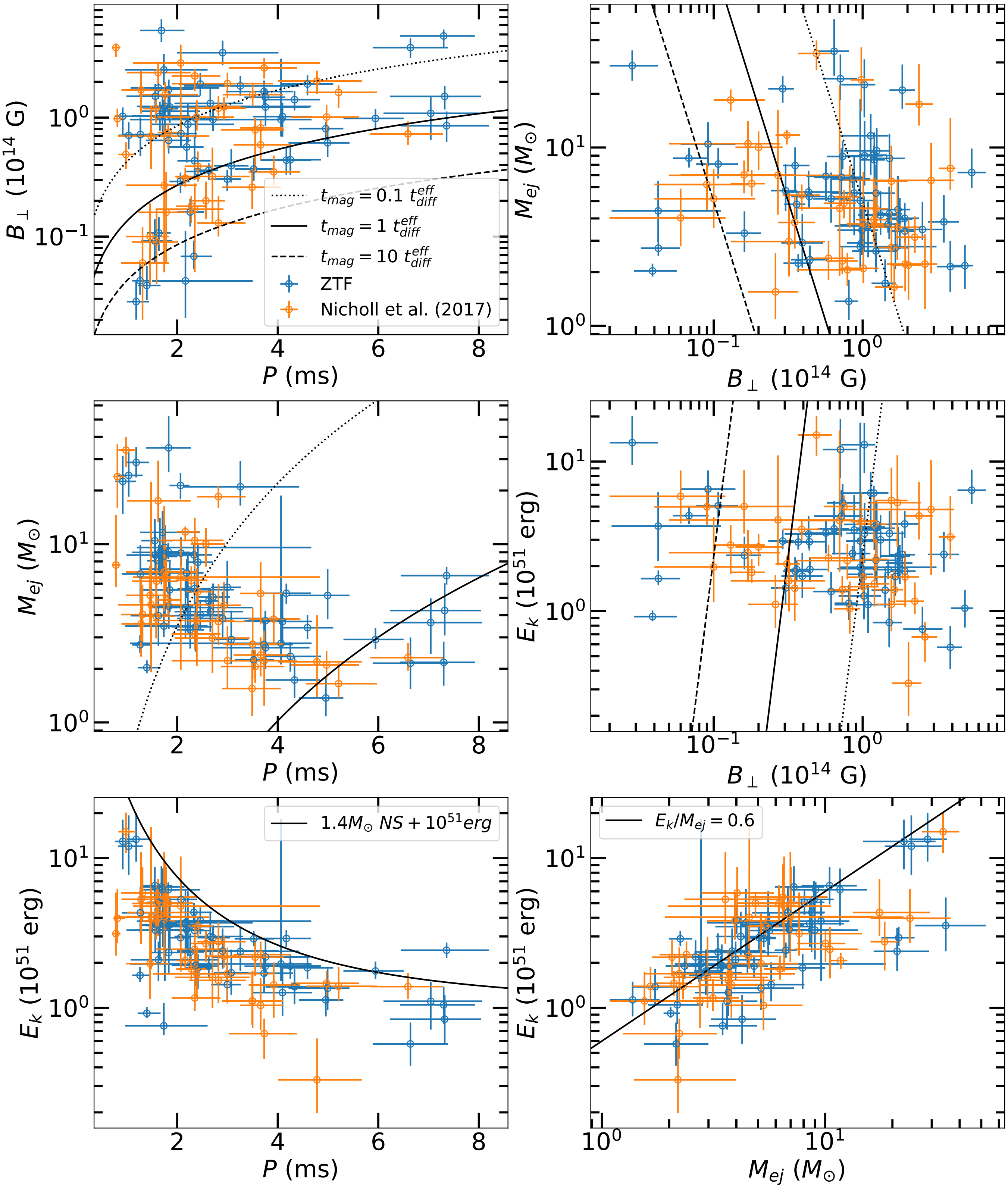

Figure A1. Values and 1σ errors of key parameters (P, $B_\perp$, M_{ej}, E_k) for the 9 SLSNe-I favored by magnetar models and the 47 equally well-fit ones. The values from our sample are marked in blue while those from Nicholl et al. (2017b) are marked in orange. t_{mag} is the spin-down time scale for the magnetar model and the ratio of t_{mag}/t_{diff}^{eff} follows Nicholl et al. (2017b, their equation 11).

REFERENCES

Anderson, J. P., Pessi, P. J., Dessart, L., et al. 2018, A&A, 620, A67, doi: 10.1051/0004-6361/201833725

Angus, C. R., Smith, M., Sullivan, M., et al. 2019, MNRAS, 487, 2215, doi: 10.1093/mnras/stz1321

Arnett, W. D. 1982, ApJ, 253, 785, doi: 10.1086/159681

Barbarino, C., Sollerman, J., Taddia, F., et al. 2021, A&A, 651, A81, doi: 10.1051/0004-6361/202038890

Barkat, Z., Rakavy, G., & Sack, N. 1967, PhRvL, 18, 379, doi: 10.1103/PhysRevLett.18.379

Bellm, E. C., Kulkarni, S. R., Graham, M. J., et al. 2019a, PASP, 131, 018002, doi: 10.1088/1538-3873/aaecbe

Bellm, E. C., Kulkarni, S. R., Barlow, T., et al. 2019b, PASP, 131, 068003, doi: 10.1088/1538-3873/ab0c2a

Benetti, S., Nicholl, M., Cappellaro, E., et al. 2014, MNRAS, 441, 289, doi: 10.1093/mnras/stu538

Blanchard, P. K., Berger, E., Nicholl, M., & Villar, V. A. 2020, ApJ, 897, 114, doi: 10.3847/1538-4357/ab9638

Bressan, A., Marigo, P., Girardi, L., et al. 2012, MNRAS, 427, 127, doi: 10.1111/j.1365-2966.2012.21948.x

Chatzopoulos, E., Wheeler, J. C., & Vinko, J. 2012, ApJ, 746, 121, doi: 10.1088/0004-637X/746/2/121

Chatzopoulos, E., Wheeler, J. C., Vinko, J., Horvath, Z. L., & Nagy, A. 2013, ApJ, 773, 76, doi: 10.1088/0004-637X/773/1/76

Chen, K.-J., Woosley, S. E., & Whalen, D. J. 2020, ApJ, 893, 99, doi: 10.3847/1538-4357/ab7db0

Chevalier, R. A., & Irwin, C. M. 2011, ApJL, 729, L6, doi: 10.1088/2041-8205/729/1/L6

De Cia, A., Gal-Yam, A., Rubin, A., et al. 2018, ApJ, 860, 100, doi: 10.3847/1538-4357/aab9b6

Dessart, L. 2019, A&A, 621, A141, doi: 10.1051/0004-6361/201834535

Dexter, J., & Kasen, D. 2013, ApJ, 772, 30, doi: 10.1088/0004-637X/772/1/30

Gal-Yam, A. 2019, ApJ, 882, 102, doi: 10.3847/1538-4357/ab2f79

Gehrels, N. 1986, ApJ, 303, 336, doi: 10.1086/164079

Graham, M. J., Kulkarni, S. R., Bellm, E. C., et al. 2019, PASP, 131, 078001, doi: 10.1088/1538-3873/ab006c

Guillochon, J., Nicholl, M., Villar, V. A., et al. 2018, ApJS, 236, 6, doi: 10.3847/1538-4365/aab761

Hosseinzadeh, G., Berger, E., Metzger, B. D., et al. 2021, arXiv e-prints, arXiv:2109.09743. https://arxiv.org/abs/2109.09743

Hsu, B., Hosseinzadeh, G., & Berger, E. 2021, ApJ, 921, 180, doi: 10.3847/1538-4357/ac1aca

Inserra, C. 2019, Nature Astronomy, 3, 697, doi: 10.1038/s41550-019-0854-4

Inserra, C., Smartt, S. J., Jerkstrand, A., et al. 2013, ApJ, 770, 128, doi: 10.1088/0004-637X/770/2/128

Kaplan, N., & Soker, N. 2020, MNRAS, 494, 5909, doi: 10.1093/mnras/staa1201

Kasen, D., & Bildsten, L. 2010, ApJ, 717, 245, doi: 10.1088/0004-637X/717/1/245

Kasen, D., Metzger, B. D., & Bildsten, L. 2016, ApJ, 821, 36, doi: 10.3847/0004-637X/821/1/36

Lattimer, J. M., & Prakash, M. 2007, PhR, 442, 109, doi: 10.1016/j.physrep.2007.02.003

Leloudas, G., Chatzopoulos, E., Dilday, B., et al. 2012, A&A, 541, A129, doi: 10.1051/0004-6361/201118498

Li, L., Wang, S.-Q., Liu, L.-D., et al. 2020, ApJ, 891, 98, doi: 10.3847/1538-4357/ab718d

Liu, L.-D., Gao, H., Wang, X.-F., & Yang, S. 2021, ApJ, 911, 142, doi: 10.3847/1538-4357/abf042

Liu, L.-D., Wang, L.-J., Wang, S.-Q., & Dai, Z.-G. 2017a, arXiv e-prints, arXiv:1706.01783. https://arxiv.org/abs/1706.01783

Liu, Y.-Q., Modjaz, M., & Bianco, F. B. 2017b, ApJ, 845, 85, doi: 10.3847/1538-4357/aa7f74

Liu, Y.-Q., Modjaz, M., Bianco, F. B., & Graur, O. 2016, ApJ, 827, 90, doi: 10.3847/0004-637X/827/2/90

Lunnan, R., Fransson, C., Vreeswijk, P. M., et al. 2018, Nature Astronomy, 2, 887, doi: 10.1038/s41550-018-0568-z

Lunnan, R., Yan, L., Perley, D. A., et al. 2020, ApJ, 901, 61, doi: 10.3847/1538-4357/abaeec

Lyman, J. D., Bersier, D., James, P. A., et al. 2016, MNRAS, 457, 328, doi: 10.1093/mnras/stv2983

Margutti, R., Metzger, B. D., Chornock, R., et al. 2017, ApJ, 836, 25, doi: 10.3847/1538-4357/836/1/25

Masci, F. J., Laher, R. R., Rusholme, B., et al. 2019, PASP, 131, 018003, doi: 10.1088/1538-3873/aae8ac

Modjaz, M., Liu, Y. Q., Bianco, F. B., & Graur, O. 2016, ApJ, 832, 108, doi: 10.3847/0004-637X/832/2/108

Moriya, T. J., Blinnikov, S. I., Tominaga, N., et al. 2013, MNRAS, 428, 1020, doi: 10.1093/mnras/sts075

Moriya, T. J., & Maeda, K. 2012, ApJL, 756, L22, doi: 10.1088/2041-8205/756/1/L22

Nicholl, M., Berger, E., Margutti, R., et al. 2017a, ApJL, 845, L8, doi: 10.3847/2041-8213/aa82b1

Nicholl, M., Guillochon, J., & Berger, E. 2017b, ApJ, 850, 55, doi: 10.3847/1538-4357/aa9334

Nicholl, M., & Smartt, S. J. 2016, MNRAS, 457, L79, doi: 10.1093/mnrasl/slv210

Nicholl, M., Smartt, S. J., Jerkstrand, A., et al. 2013, Nature, 502, 346, doi: 10.1038/nature12569

—. 2015a, ApJL, 807, L18, doi: 10.1088/2041-8205/807/1/L18
—. 2015b, MNRAS, 452, 3869, doi: 10.1093/mnras/stv1522
Nicholl, M., Berger, E., Smartt, S. J., et al. 2016, ApJ, 826, 39, doi: 10.3847/0004-637X/826/1/39
Nyholm, A., Sollerman, J., Tartaglia, L., et al. 2020, A&A, 637, A73, doi: 10.1051/0004-6361/201936097
Ofek, E. O., Cameron, P. B., Kasliwal, M. M., et al. 2007, ApJL, 659, L13, doi: 10.1086/516749
Oke, J. B., & Gunn, J. E. 1983, ApJ, 266, 713, doi: 10.1086/160817
Oke, J. B., Cohen, J. G., Carr, M., et al. 1995, PASP, 107, 375, doi: 10.1086/133562
Pedregosa, F., Varoquaux, G., Gramfort, A., et al. 2011, Journal of Machine Learning Research, 12, 2825
Piro, A. L. 2015, ApJL, 808, L51, doi: 10.1088/2041-8205/808/2/L51
Planck Collaboration, Ade, P. A. R., Aghanim, N., et al. 2016, A&A, 594, A13, doi: 10.1051/0004-6361/201525830
Prentice, S. J., Mazzali, P. A., Pian, E., et al. 2016, MNRAS, 458, 2973, doi: 10.1093/mnras/stw299
Quataert, E., Lecoanet, D., & Coughlin, E. R. 2019, MNRAS, 485, L83, doi: 10.1093/mnrasl/slz031
Quimby, R. M., Aldering, G., Wheeler, J. C., et al. 2007, ApJL, 668, L99, doi: 10.1086/522862
Quimby, R. M., Kulkarni, S. R., Kasliwal, M. M., et al. 2011, Nature, 474, 487, doi: 10.1038/nature10095
Quimby, R. M., De Cia, A., Gal-Yam, A., et al. 2018, ApJ, 855, 2, doi: 10.3847/1538-4357/aaac2f
Rakavy, G., & Shaviv, G. 1967, ApJ, 148, 803, doi: 10.1086/149204
Roming, P. W. A., Kennedy, T. E., Mason, K. O., et al. 2005, SSRv, 120, 95, doi: 10.1007/s11214-005-5095-4
Ryder, S. D., Sadler, E. M., Subrahmanyan, R., et al. 2004, MNRAS, 349, 1093, doi: 10.1111/j.1365-2966.2004.07589.x
Smith, M., Sullivan, M., D'Andrea, C. B., et al. 2016, ApJL, 818, L8, doi: 10.3847/2041-8205/818/1/L8
Smith, N., Li, W., Foley, R. J., et al. 2007, ApJ, 666, 1116, doi: 10.1086/519949
Sorokina, E., Blinnikov, S., Nomoto, K., Quimby, R., & Tolstov, A. 2016, ApJ, 829, 17, doi: 10.3847/0004-637X/829/1/17
Speagle, J. S. 2020, MNRAS, 493, 3132, doi: 10.1093/mnras/staa278
Taddia, F., Sollerman, J., Fremling, C., et al. 2019, A&A, 621, A71, doi: 10.1051/0004-6361/201834429
Terreran, G., Blanchard, P., DeMarchi, L., et al. 2020, The Astronomer's Telegram, 13970, 1
Vreeswijk, P. M., Leloudas, G., Gal-Yam, A., et al. 2017, ApJ, 835, 58, doi: 10.3847/1538-4357/835/1/58
Vurm, I., & Metzger, B. D. 2021, ApJ, 917, 77, doi: 10.3847/1538-4357/ac0826
Wheeler, J. C., Chatzopoulos, E., Vinkó, J., & Tuminello, R. 2017, ApJL, 851, L14, doi: 10.3847/2041-8213/aa9d84
Woosley, S. E. 2010, ApJL, 719, L204, doi: 10.1088/2041-8205/719/2/L204
—. 2017, ApJ, 836, 244, doi: 10.3847/1538-4357/836/2/244
Woosley, S. E., Blinnikov, S., & Heger, A. 2007, Nature, 450, 390, doi: 10.1038/nature06333
Yan, L., Quimby, R., Ofek, E., et al. 2015, ApJ, 814, 108, doi: 10.1088/0004-637X/814/2/108
Yan, L., Quimby, R., Gal-Yam, A., et al. 2017a, ApJ, 840, 57, doi: 10.3847/1538-4357/aa6b02
Yan, L., Lunnan, R., Perley, D. A., et al. 2017b, ApJ, 848, 6, doi: 10.3847/1538-4357/aa8993
Yan, L., Perley, D. A., Schulze, S., et al. 2020, ApJL, 902, L8, doi: 10.3847/2041-8213/abb8c5